PAPER • OPEN ACCESS

Turbulence-reduced high-performance scenarios in Wendelstein 7-X

View the article online for updates and enhancements.

Turbulence-reduced high-performance scenarios in Wendelstein 7-X

O.P. Ford[1],[*] ⬤, M. Beurskens[1] ⬤, S.A. Bozhenkov[1] ⬤, S. Lazerson[1] ⬤, L. Vanó[1],
A. Alonso[2] ⬤, J. Baldzuhn[1] ⬤, C.D. Beidler[1], C. Biedermann[1], R. Burhenn[1], G. Fuchert[1] ⬤,
D. Hartmann[1] ⬤, M. Hirsch[1], A. Langenberg[1] ⬤, H. Laqua[1], P. McNeely[1], N. Pablant[3] ⬤,
E. Pasch[1], F. Reimold[1] ⬤, T. Romba[1] ⬤, N. Rust[1], R. Schroeder[1], E.R. Scott[1], T. Stange[1] ⬤,
H.M. Smith[1], D. Gradic[1] ⬤, R.C. Wolf[1] ⬤, D. Zhang[1] ⬤ and the W7-X Team[a]

[1] Max-Planck Institut für Plasmaphysik, 17491 Greifswald, Germany
[2] CIEMAT, Avenida Complutense, 40, 28040 Madrid, Spain
[3] Princeton Plasma Physics Laboratory, Princeton, NJ 08543, United States of America

E-mail: eps20(at)oliford.co.uk

CrossMark

Abstract

In the Wendelstein 7-X (W7-X) stellarator, turbulence is the dominant transport mechanism in most discharges. This leads to a 'clamping' of ion temperature over a wide range of heating power, predominantly flat density profiles where hollow profiles driven by neoclassical thermo-diffusion would be expected and by rapid impurity transport in injection experiments. Significantly reduced turbulent transport is observed in the presence of strong core density gradients found transiently after core pellet injection and irregularly after boronisation or boron pellet injection. Density peaking is also achieved in a controlled manner in purely neutral beam heated discharges where particle transport analysis reveals an abrupt reduction in the main-ion particle flux leading to significant density profile peaking not explained by the NBI particle source alone. The plasmas exhibit a heat diffusivity of around $\chi = 0.25 \pm 0.1\,\mathrm{m^2\,s^{-1}}$ at mid radius, a factor of around 4 lower than ECRH dominated discharges. Despite the improved confinement, the achieved ion temperature is limited by broader heat deposition and the lower power-per-particle given the higher density. This is overcome with limited reintroduction of ECRH power, where the low heat diffusivity diffusivity is maintained, the density rise supressed and ion temperatures above the clamping limit are achieved. The applicability of these plasmas for a high performance scenario on transport relevant time scales is assessed, including initial predictions for planned heating upgrades of W7-X, based on a range of assumptions about particle transport.

Keywords: stellarator, transport, scenarios, turbulence, neoclassical

(Some figures may appear in colour only in the online journal)

---

1. Introduction

Wendelstein 7-X (W7-X) is a superconducting 5 period helical axis stellarator optimised to reduce neoclassical losses due to helical magnetic field ripple [1–3]. Effective steady-state operation (30 min) is planned using continuous electron cyclotron resonance heating (ECRH) [4] and actively cooled targets based on the island divertor power exhaust scheme [5]. In the 2017 and 2018 operation campaigns, high-density plasmas up to 1.4×10^{20} m^{-3} [6] and steady-state operation up to 100 s [5] were reliably achieved using ECRH with gas puff fueling. In periods of improved confinement after pellet fueling [7], the neoclassical optimisation of W7-X was successfully demonstrated [8]. However, these were not achieved simultaneously, since the steady-state gas-fuelled ECRH baseline scenario was limited by strong turbulent transport and the improved confinement scenario was only achieved transiently for periods of order one energy confinement time.

2. Gas-fuelled ECRH scenario

2.1. Impurity and particle transport

Almost all gas-fuelled plasmas with ECRH power above 1 MW exhibit electron density profiles that are stable in time and either flat or very slightly peaked. Impurity density profiles in such discharges are also almost flat, with relatively low concentration [9, 10], particularly after boronisation [11].

Typical profiles are shown in figure 1 where the electron density n_e (black, a) data points are measured by Thomson scattering (TS) [12] and a single channel dispersion interferometer [13, 14]. Carbon densities n_C (green, b) are taken from charge exchange recombination spectroscopy (CXRS) measurements made during 20 ms neutral beam injection (NBI) blips [9, 15, 16]. Solid lines show simple fits performed using a moving regression based on Nadaraya–Watson kernel estimation, using a fixed scale length (n_e: $\Delta\rho \approx 0.06$, n_C: $\Delta\rho \approx 0.02$). Each data point results from a temporal average of at least 100 ms to ensure that statistical uncertainties are insignificant and these are therefore not plotted. The remaining scatter results from systematic uncertainties as discussed in detail in the referenced papers. All fits used in this work are performed in this way.

In stark contrast to the shown measured profile, there was an expectation of strongly hollow density profiles [17, 18] due to the large neoclassical thermo-diffusive force calculated for typical W7-X plasmas. To illustrate this, a simulation of the expected steady-state density profile (dashed) given entirely neoclassical particle transport is shown in figure 1(*a*). The simulation is performed using the NTSS [19] stellarator transport code based on the experimental temperature and electron density profiles and using an edge particle source function that would be required to match the experimental separatrix density $n_e(\rho = 1.0)$. To reproduce the experimental density profile using NTSS, either a strong core particle source or an anomalous flux equal but opposite to the neoclassical flux is required. The former can be excluded since only recycling and gas-fuelling is used.
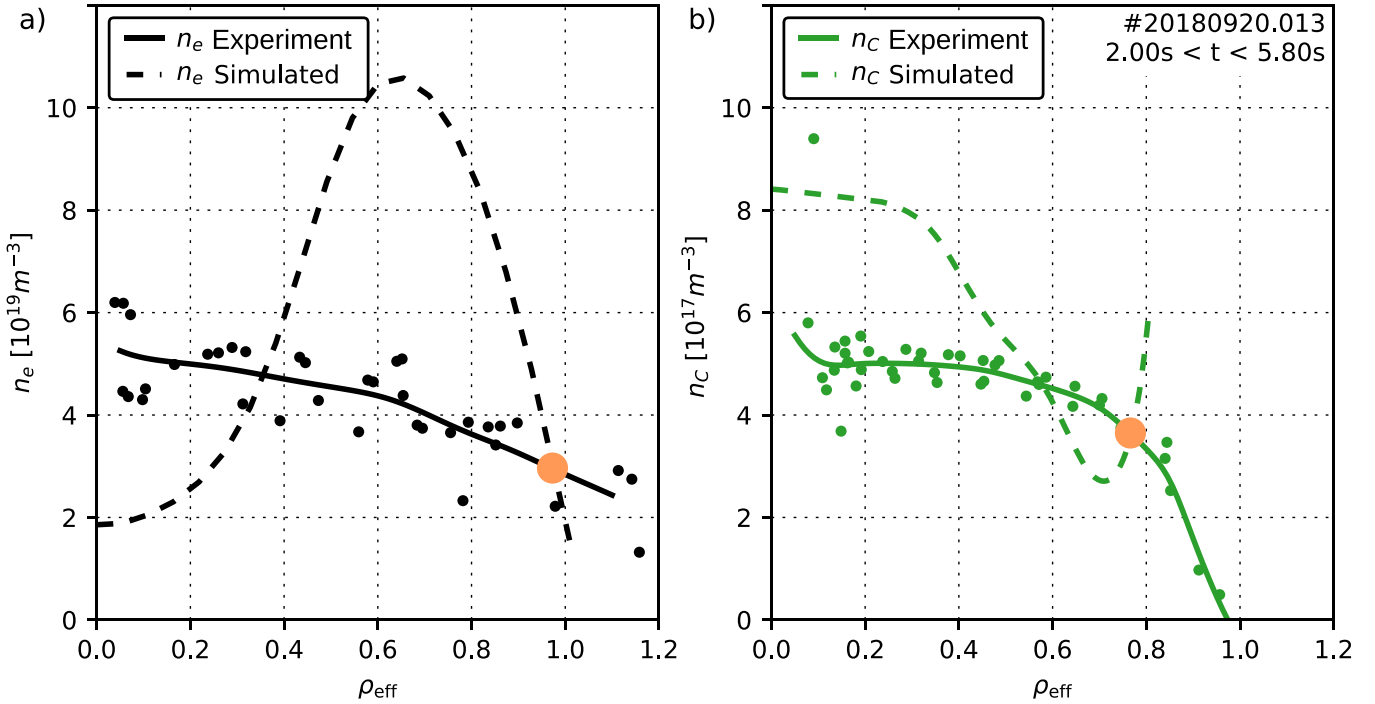
Given the flat electron density profile, neoclassical transport alone would drive impurity accumulation in these plasmas and this was expected to be a significant problem for W7-X [20]. This is illustrated in figure 1(*b*) by the result of an impurity transport simulation (dashed) using the PySTRAHL [21] code. The simulation is based on the experimental electron density and temperature profiles and impurity diffusion and convection profiles calculated by the Neotransp [22] code. Neotransp uses tabulated mono-energetic transport coefficients from DKES [23] to find a self-consistent set of diffusion, convection and radial electric field profiles, ensuring ambipolarity. A flat effective charge (Z_{eff}) profile is assumed and in PySTRAHL, a carbon source function at the edge is imposed that would be needed to match the measured edge carbon density $n_C(\rho = 0.8)$. The results of the simulation give significantly higher and more peaked impurity density than the experimental profiles with relatively little sensitivity to the input parameters. This shows that neoclassical impurity transport is not sufficient to explain the observed impurity density profiles.

The experimental impurity transport in gas-fuelled ECRH plasmas has been determined with laser-blow-off injection of trace impurities [24, 25], which allows separation of the diffusive and convective fluxes. It is found that a diffusion coefficient at least two orders of magnitude higher than the neoclassical values is observed whereas the pinch term is of a similar order of magnitude as the neoclassical calculation. Additionally, no strong dependence of the impurity transport with charge is observed, as would be expected if neoclassical impurity transport were significant [26].

Introducing a similarly strong turbulent diffusion in the main ion particle transport as is measured for the impurities is not sufficient to explain the slightly peaked electron density profile. It would give a marginally hollow profile approaching flat and would require a particle source rate significantly higher than those expected from EMC3-EIRENE simulations [27] or seen in recycling fluxes calculated from measurements by H_α imaging [28]. These observations indicate the presence of a strong anomalous pinch, counteracting the neoclassical flux. A strong anomalous pinch was also observed in W7-AS [29, 30], although there was no confirmed theoretical understanding of this.

2.2. Heat transport

The majority of ECRH heated gas-fuelled plasmas in W7-X are dominated by turbulent heat transport [31, 32], leading to an effective limit to the achievable ion temperature of 1.6 keV. This can be seen in figure 3(*b*), which shows the central electron and ion temperatures of gas-fuelled plasmas (small points) in the 2018 W7-X operational campaign over a wide range of ECRH power and collisionality. Electron temperatures are the average over data points from the TS diagnostic within $\rho < 0.2$ and ion temperatures are the average of inverted profiles from x-ray crystal imaging spectroscopy [33]. An offset of -200 eV is applied to the inverted T_i profiles, determined from campaign-wide database comparison with CXRS

Figure 1. Observed (*a*) electron and (*b*) carbon density data (points) and profiles (solid) in typical steady-state gas-fuelled and centrally ECRH heated W7-X plasmas. Dashed profiles show simulated (*a*) electron density profiles assuming neoclassical particle transport given the experimental temperature profiles and (*b*) carbon density profiles assuming neoclassical impurity transport given experimental electron density and temperature profiles.

measurements. The color scale shows the ratio of the electron-ion collision time $\tau_{\rm ei}$ to the energy confinement time $\tau_{\rm E}$.

At low electron-ion collisionality ($\tau_{\rm ei}/\tau_{\rm E} > 1.5$), limited transfer of energy to the ions explains the low $T_{\rm i}$ values but at moderate densities and powers, the species coupling should be sufficient to significantly heat the ions. Simulations with only neoclassical transport [31] (black diamonds) show that at least $T_{\rm i} > 2.5$ keV should be achievable. Instead, strong ITG turbulence [34, 35] leads to a rapidly increasing ion heat flux for only small changes in $\nabla T_{\rm i}$. This is exacerbated by a further increase of turbulence with the rising $T_{\rm e}/T_{\rm i}$ ratio [31] and leads to the observed ion temperature clamping limit regardless of the heating power applied. Under the assumption of dominant neoclassical transport, ion temperatures would be expected to reach around 4 keV with 8 MW of O2 heating [19], giving a global energy confinement time τ_E above the ISS04 scaling [36]. The observed plasmas are instead below the scaling and do not extrapolate easily to a viable reactor design so would require further optimisation to reduce turbulence [37].

Taken together, all transport channels including both heat and particles give a consistent picture of strong anomalous transport in the baseline gas-fuelled and ECRH heated scenario. For the main ion and impurity particles, this is beneficial, allowing easy fuelling of the core plasma and avoiding impurity accumulation which would be problematic under pure neoclassical conditions. However, it presents a significant problem for the heat transport and viability of a W7-X like reactor design.

3. Suppressed turbulence scenarios

Fortunately, the first campaign also showed several cases where this turbulence is strongly reduced. This is seen in some cases directly as improved performance ($T_{\rm i}$ and $\tau_{\rm E}$) as well as reduced particle and impurity transport.

3.1. Post-pellet high performance plasmas

Suppressed turbulence is seen immediately after the injection of a rapid series of hydrogen ice pellets [7, 38] when the central ion temperature climbs to a peak of around 3 keV, well above the 1.6 keV clamping limit. Figure 2 shows the density and temperature profiles at this peak (solid) and in a later phase of the discharge with the same heating power but no pellet fuelling (dashed). In the region $0.3 < \rho < 0.7$, a strong density gradient forms, which is approximately coincident with a significant steepening of the ion temperature gradient (figure 2(*b*), blue). A detailed transport analysis of a similar discharge [7] shows that the ion heat flux is reduced to the order of the calculated neoclassical flux while the electron heat flux remains dominated by turbulent transport. The proposed mechanism for the reduction is the suppression of ITG turbulence by the steep density gradient [39]. Strong TEM turbulence is not driven by steep density gradient as these are generally suppressed in this magnetic configuration of W7-X [40]. This leads to a favourable region of operational space with low turbulence known as the 'stability valley' [41], which is
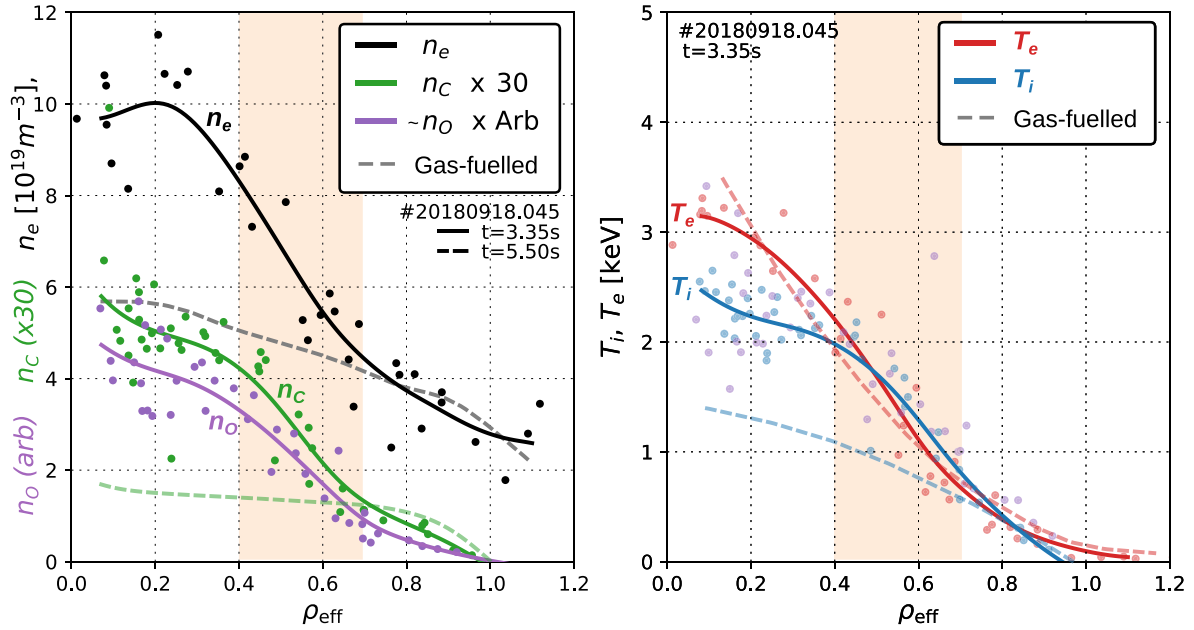
Figure 2. (*a*) Electron (black), carbon (green) and oxygen (purple) density profiles during a high performance phase after pellet injection (solid) and in matching conditions without pellet injection (dashed). (*b*) Electron (red) and ion (blue) temperature profiles in the same cases. Oxygen profiles are arbitrarily scaled as validated charge exchange rate coefficients are not yet available. Ion temperatures derived from the oxygen charge exchange emission (purple dots) are also included in the T_i fit. The region of steep gradients is highlighted in orange.

supported by measurements of reduced turbulent fluctuations [42, 43].

The carbon and oxygen density profile shapes measured by the CXRS diagnostic are also shown in figure 2(*a*). These show strong gradients after the pellet injection approximately coincident with the gradient region of the electron density profile. The appearance of a strong gradient in impurities where the only source is at the plasma edge indicates the presence of a strong inward convection term. This is also seen in an analysis of argon impurity transport using the x-ray crystal spectrometer [44]. Although the core impurity levels do peak significantly in this phase, the absolute levels remain low and indicate a peak effective charge of at most $Z_{eff} \approx 1.5$ [9]. However, it should be noted that the longest post-pellet phase seen lasted only ≈ 0.5 s and the impurity densities do not reach a steady-state, so it is not yet clear if the impurities would continue to accumulate if the density gradient could be sustained.

Figure 3(*b*) shows the peak performance phase of all such discharges in the last campaign (stars), with core T_i values well above the $T_i \leqslant 1.6$ keV limit and approaching the largely neoclassical transport simulations (black diamonds). They represent an attractive scenario with confinement that lies slightly above the ISS04 scaling which is typically used in stellarator reactor designs [45]. However, the density gradient and turbulence suppression has so far been only transient and vanishes after a short time as the core density relaxes. Figure 3(*a*) shows the time traces of the main plasma parameters as well as the normalised density gradient $a/L_n = \frac{1}{n_e} \frac{dn_e}{d\rho}$ at the steepest location (green). The fall-off of this density gradient at $t > 2.6$ s is shortly followed by the return of strong turbulent transport

and the fall of T_i back to around 1.6 keV. A steady-state pellet injector [46] will be installed in a future experimental campaign and experiments will investigate if the favourable conditions can be maintained. However, it can be seen in figure 3(*a*) that while the average density (black) rises significantly during the pellet injection, the normalised gradient rises only after the injection of the last pellet due to the edge density receding more rapidly than the core. It is likely to prove difficult to achieve the necessary core/edge density ratio with a continuous stream of pellets.

Figure 3(*b*) also shows a small number of discharges (green triangles) where a similar effect was achieved with the injection of a 'TESPEL' pellet consisting of a small plastic ball containing a small amount of high-Z impurity.

3.2. Post-boronisation, low-power scenario

A class of plasma that clearly exceed the $T_i \leqslant 1.6$ keV clamping limit is seen immediately after boronisation [11] of the first wall and with low ECRH power $P_{ECRH} < 1.5$ MW. Figure 4(*a*) shows the density and ion temperature profiles (solid) compared to those from a similar high-power ECRH discharge later in the 2018 campaign (dashed). The increased T_i gradients are again consistent with the region of steep ∇n_e, which in this case appears with a strongly reduced separatrix density. Although the achieved T_i is only moderately above the normal limit, as seen in figure 4(*b*) (squares), the very low ECRH power leads to a relatively high τ_E. While encouraging, this is of limited value if it occurs only at low powers and would therefore not be scalable to a reactor scenario. Additionally,
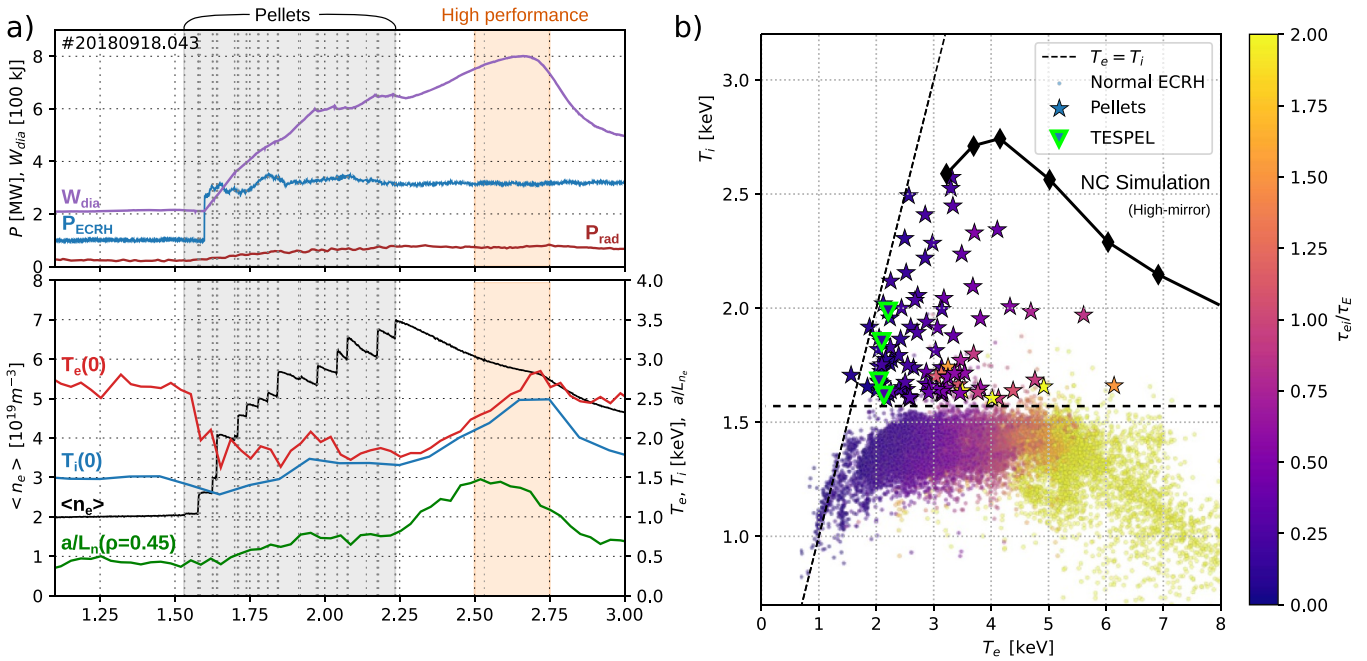
Figure 3. (*a*) Time traces of main plasma parameters through pellet injection (gray) and high performance (orange) phases. (*b*) Scatter plot of core ion vs electron temperature for ECRH heated gas-fuelled (small points) and pellet-fuelled (stars) plasmas in the 2018 experiment campaign. The color scale shows the electron-ion equilibration time relative to the energy confinement time. Black diamonds show the expectation from transport simulations [31] assuming only neoclassical heat transport for the high-mirror magnetic configurations.
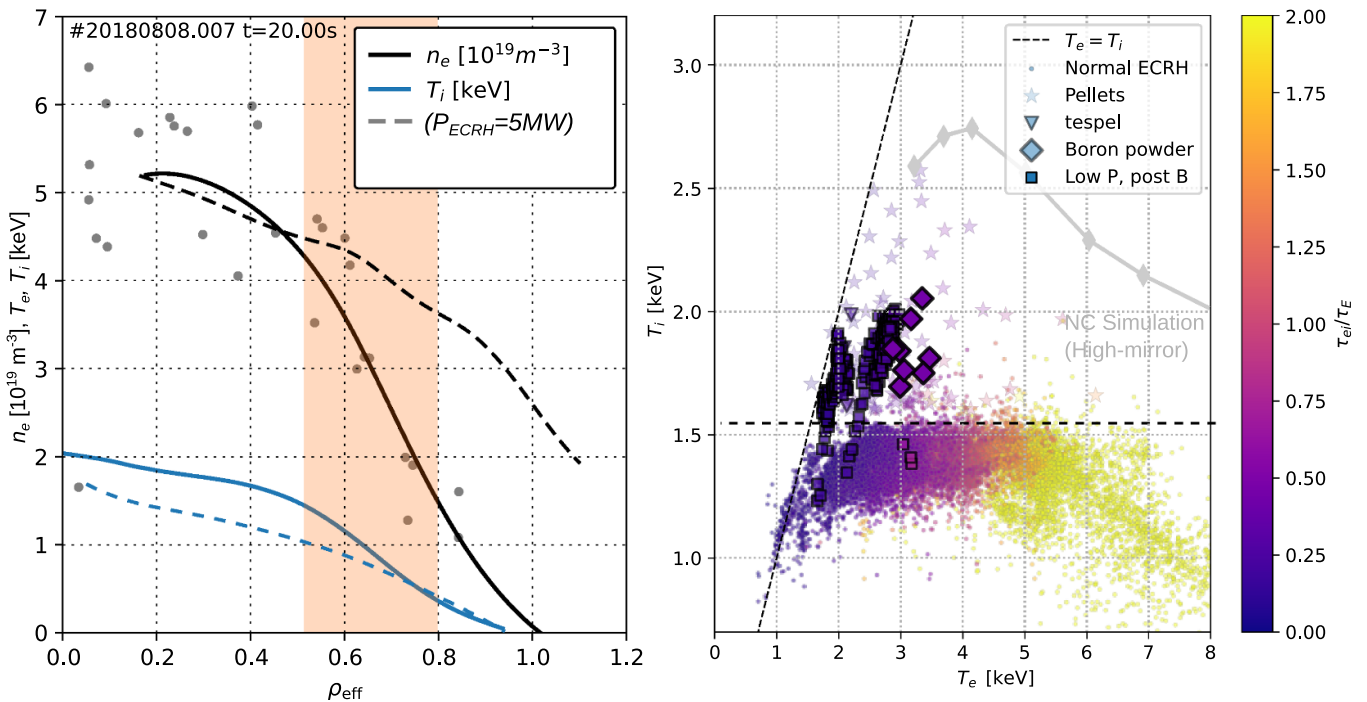
Figure 4. (*a*) Profiles of electron density (black) and ion temperature (blue) in a low ECRH power discharge after boronisation (solid) compared with similar density high-power discharge (dashed). (*b*) Scatter plot of core ion vs electron temperature as figure 2(*b*) including low-power post-boronisation plasmas (squares) and boron dropper experiments [48] (diamonds).

a requirement of a very low separatrix density may make the scenario incompatible with good power and particle exhaust. On the other hand these plasmas were each maintained with elevated T_i for over 30 s, making them inherently steady-state relevant. Unfortunately, only two such plasmas were observed

in the 2018 campaign and while these could be reproduced in the 2022/3 campaign, the required set of conditions for this scenario to occur are not yet known as the majority of experiments are conducted at higher ECRH power. Accumulation of impurities in the plasma core is observed due the reduction

of impurity flux towards neoclassical levels [47], indicating a strong reduction in turbulent transport.

3.3. Boron powder injection

A similar effect was seen after massive injections of boron into the scrape-off layer with a boron powder dropper [48]. At the largest injection quantities, a reduction of the scrape-off layer density is coupled with increased density in the core correlated with the injections. The combined density gradient leads to an improved T_i, as shown in figure 4(*b*) (diamonds). While the effect was seen only with the largest quantity of Boron and hence produced a highly dynamic plasma, the apparent ability of the boron dropper to influence the separatrix density makes it of interest as a possible density profile actuator.

4. Scenarios with NBI heating

Since steep density gradients are evidently the critical ingredient for achieving $T_i > 1.6$ keV, the most direct way to create these in steady state would be with direct continuous core fuelling by NBI. During the 2018 experimental campaign, two new positive ion neutral injector (PINI) sources were commissioned [49, 50]. Together, the sources provided approximately 2.6 MW of mixed ion and electron heating [51, 52] as well as 4×10^{20} particles s^{-1} fuelling. Due to the near radial injection and hence short interaction length compared to the large volume of W7-X plasmas, the NBI system cannot provide plasma start-up at W7-X [53] so the majority of NBI operation was conducted in gas-fuelled plasmas with significant ECRH. The high turbulence levels of these plasmas is unchanged by the introduction of NBI and the additional power has almost no effect on T_i. This is seen in figure 5(*a*) which shows all NBI and NBI+ECRH discharges in the T_i vs T_e space as before, with the majority remaining at or below the $T_i \leqslant 1.6$ keV limit. In general, the points can be split into two branches. The first branch lies along the $T_i = T_e$ line, which are pure NBI and/or very high density discharges with high collisionality and strong electron-ion coupling. The second branch, with $T_e > T_i$, are mixed NBI+ECRH plasmas. Of most interest are the small number of plasmas seen above the T_i limit in each branch, which correspond to plasmas with the lowest ECRH power. The effect is clearer in figure 5(*b*) which shows the same data set in terms of the global energy confinement τ_E vs the total heating power. The color scale gives the ECRH power only. A clear change in trend can be seen at around $P_{\mathrm{ECRH}} \approx 1$ MW ($P_{\mathrm{tot}} \approx 3.5$ MW). Above this, with higher ECRH powers, the NBI+ECRH data follows the background cloud of ECRH data points, consistent with the typical ITG dominated scenario. For $P_{\mathrm{ECRH}} < 1$ MW, the performance is notably improved, with the pure NBI plasmas showing the best relative performance, albeit at low total power.

One particular discharge, #181009.034, includes a phase of mixed 2.5 MW NBI + 1.1 MW O2-mode ECRH and appears notably above the others in τ_E. This plasma sits amongst the highest points on the $T_e = T_i$ line in figure 5(*a*). The time trace of this discharge is s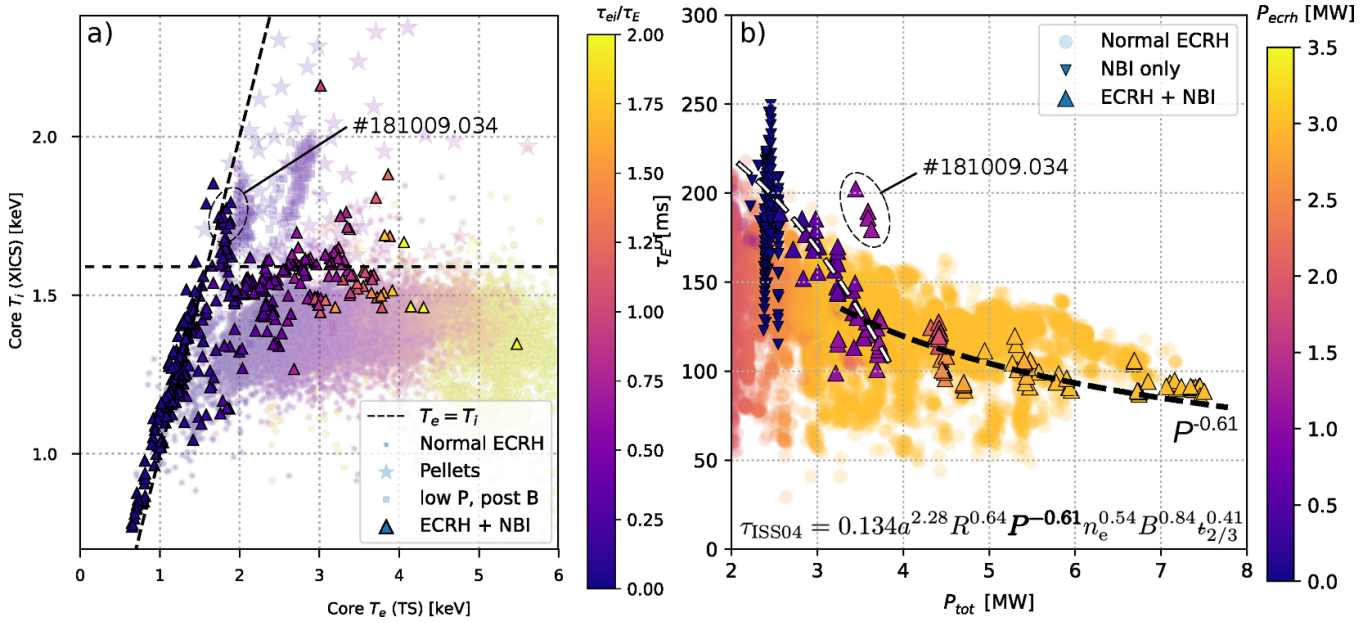hown in figure 6 and the profiles derived from time averages of the highlighted regions marked A to D are shown in figure 7. The plasma is started with 2 MW of X2-mode ECRH heating and gas fuelling and achieves a typical ITG-dominated plasma with high electron and limited ion temperature at moderate density before switching to 2.5 MW of pure-NBI heating. The NBI heating has a very broad profile of mixed electron-ion heating, slightly biased towards ions in the core and towards electrons near the edge [54]. The removal of the concentrated on-axis ECRH at the transisiton to pure NBI heating causes a decrease of the central electron temperature to equal to that of the ions (A). During the first 1 s of the pure NBI heating (A–B), both temperatures rise slightly and saturate at 1.3 keV, the density peaks slightly and the carbon density remains flat. At around $t = 2$ s, with no evident external changes, the central electron and carbon densities begin to rise rapidly, achieving strongly peaked n_e and n_C profiles just before the end of the NBI only phase (C). This peaking occurs only inside $\rho < 0.5$, with little change to the profiles outside of mid radius. With the introduction of an additional 1 MW of O2-mode ECRH at $t = 3$ s, the temperatures rises rapidly, with T_i peaking at 1.75 keV, marginally but measurably above the 1.6 keV limit. The core electron density rise stops and the peaking reduces over 500 ms. In this time, the core temperatures also relax back to around the value of the normal limit. While the global behaviour is reminiscent of the post-pellet high performance discharges, and indeed the final T_i profile (D in figure 7) does show a steeper T_i gradient around the location of the steepest n_e gradient (yellow highlight), the temperature differences are small and a full heat transport analysis is required to determine if the turbulence is in fact reduced compared to a typical discharge with only ECRH. The most remarkable effect of the reintroduction of the ECRH however is the rapid reduction of the core electron and carbon densities. The final carbon profile (D, green) is noticeably flatter within $\rho < 0.3$, coincident with the ECRH deposition region (dark-red in figure 7(*c*)). While the electron density is also reduced in the very core, indicating a reduction in ∇n_e, the signal to noise ratio of the TS data requires a stronger smoothing constraint to fit and so it is not clear if the lower gradient is also exactly coincident with the deposition region.

Using this plasma discharge, the heat and particle transport in three specific scenarios can be examined and compared: (1) ECRH or ECRH dominated (>2 MW) plasmas with or without NBI, (2) pure NBI plasmas, (3) Density-peaked NBI plasmas with low ECRH heating ($\leqslant 1$ MW).

4.1. Particle transport

The anomalous particle flux $\Gamma_a(\rho)$ is assessed by subtracting calculated neoclassical fluxes Γ_{NC} from the experimental particle flux Γ. This can be calculated from the volume integral of all sources and sinks $S_{\mathrm{e,i}}$ and the change in the electron density enclosed by that surface:

$$\Gamma_{\mathrm{e,i}}(\rho) = \int_0^\rho \left(S_{e,i}(\rho') - \frac{\mathrm{d}n_e(\rho')}{\mathrm{d}t} \right) \frac{\mathrm{d}V(\rho')}{\mathrm{d}\rho'} \mathrm{d}\rho'. \quad (1)$$

Figure 5. Scatter plots of (*a*) core ion vs electron temperature as figure 2(*b*) including all NBI and mixed NBI+ECRH plasmas (triangles). (*b*) Scatter plot of energy confinement time τ_E vs total heating power for ECRH (point cloud) and NBI or NBI+ECRH (triangles). A trend of $P^{-0.61}$, matching the ISS04 power scaling [36] is also shown in comparison to mixed NBI+ECRH discharges.
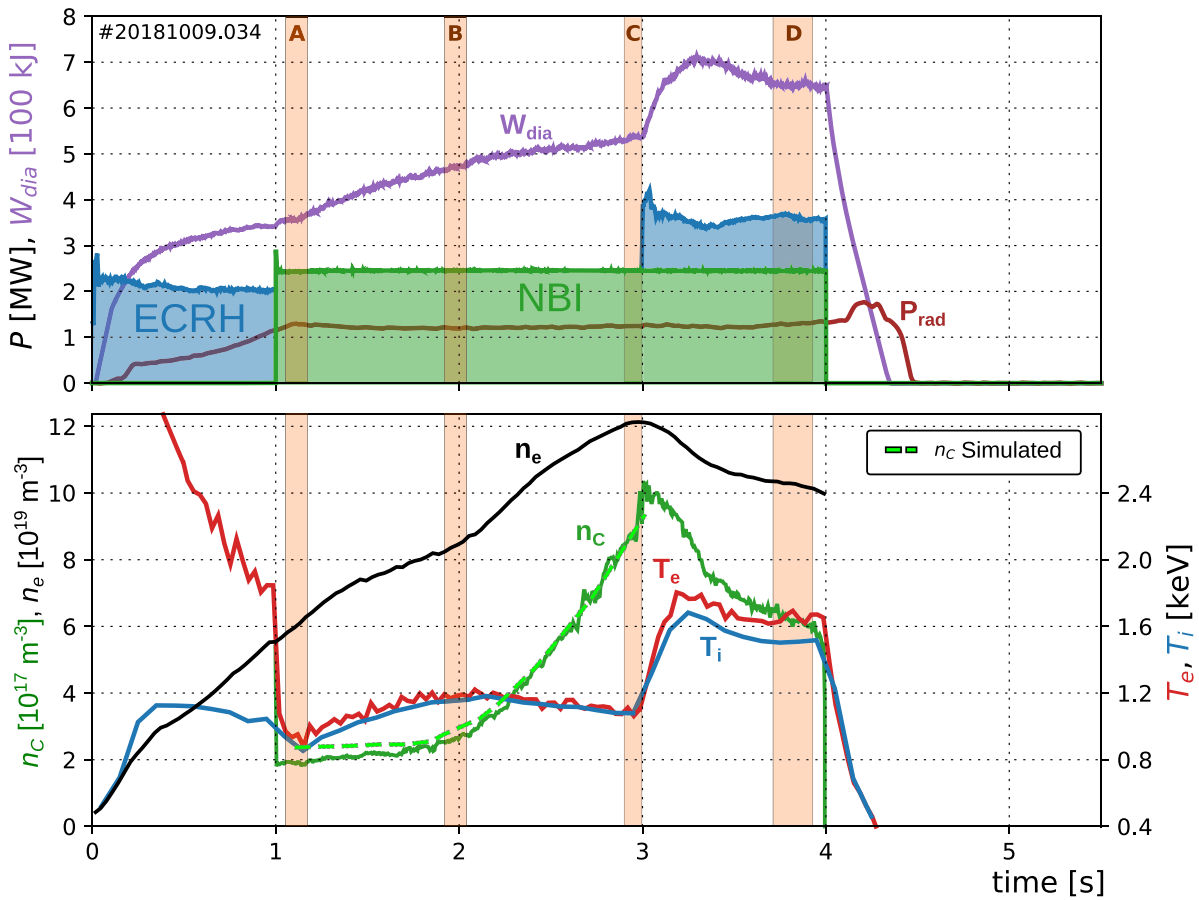
Figure 6. Time traces of global powers and energy (top) and densities and temperatures (bottom) for discharge #20181009.034 which included phases of ECRH X2, NBI and mixed NBI + ECRH O2 heating. The averaged time range of the profiles shown in figure 7 are highlighted in orange. Also shown is the core carbon density (dashed green) from transport simulations assuming only neoclassical transport during the pure-NBI phase.
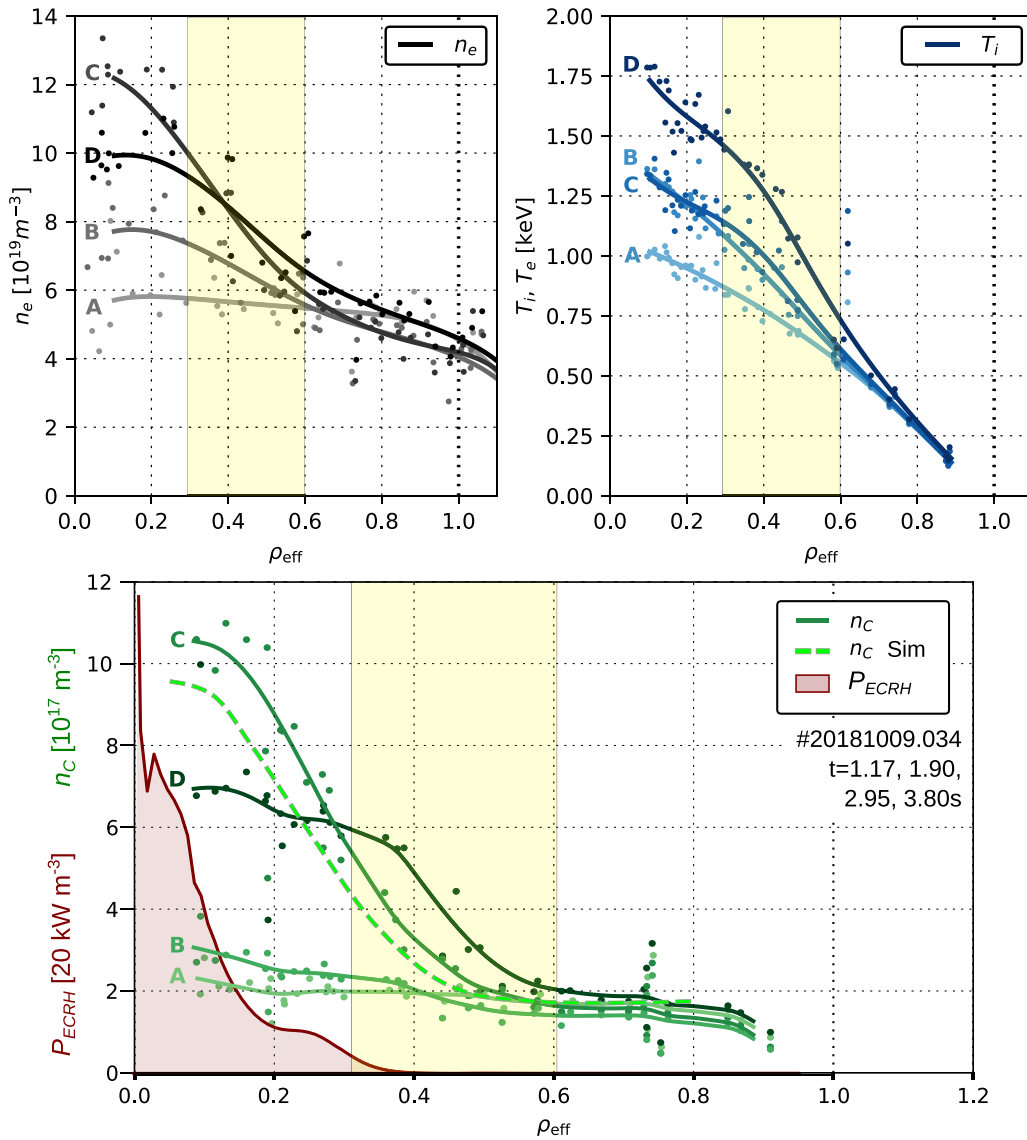
Figure 7. Electron density (*a*), ion temperature (*b*) and carbon density (*c*) profiles at selected points in discharge #20181009.034. The profiles are averaged over the time windows A,B,C and D shown in figure 6. The O2 ECRH deposition profile in red (*c*) and the region of strongest density gradient is highlighted in yellow. A simulation of the expected carbon density profile is shown as a dashed green line in (*c*) for time point C assuming only neoclassical transport.

For the gas and recycling sources, estimates of the total hydrogen neutral fluxes from the walls and divertor are available from the H_α video diagnostic [28] in some cases. In general, EMC3-EIRENE simulations [27] consistent with these show that ionisation of recycling neutrals is significant to the particle balance only nearer the plasma edge ($\rho \geqslant 0.8$). This is further supported by a few individual examples where neutral density estimations are available based on the high energy wings of the H_α spectrum [27, 31, 55]. Inside this, it can be assumed that neutral density is low and an approximate balance of recombination and ionisation gives no significant source from background neutrals.

The core particle source from NBI is calculated by Monte-carlo simulations of the attenuation of the neutral beam current through the plasma using the PyFIDASim [21, 56] and Beams3D [57] codes. These both include a detailed

model of the neutral beam duct loses and have been validated against intensity calibrated beam emission spectroscopy (BES) measurements [54, 56] to ensure total particle count and energy component fractions are correct.

The PyFidaSim source rate includes the ionisation rate of both beam neutrals and beam 'halo' neutrals, which are created by charge exchange and diffuse through the plasma before their eventual ionisation. The halo contribution is significant (around 50%) but in moderate or high density plasmas has a similar source profile to the direct ionisation due to the small diffusion length (~ 10 cm) compared to the plasma radius (50 cm) [58]. It can therefore be assumed, as it is in Beams3D, that the source rate is locally equal to the sum of the ionisation and charge exchange rates (also known as the beam-stopping rate). This is confirmed by a good match of Beams3D and PyFIDASim source profiles.
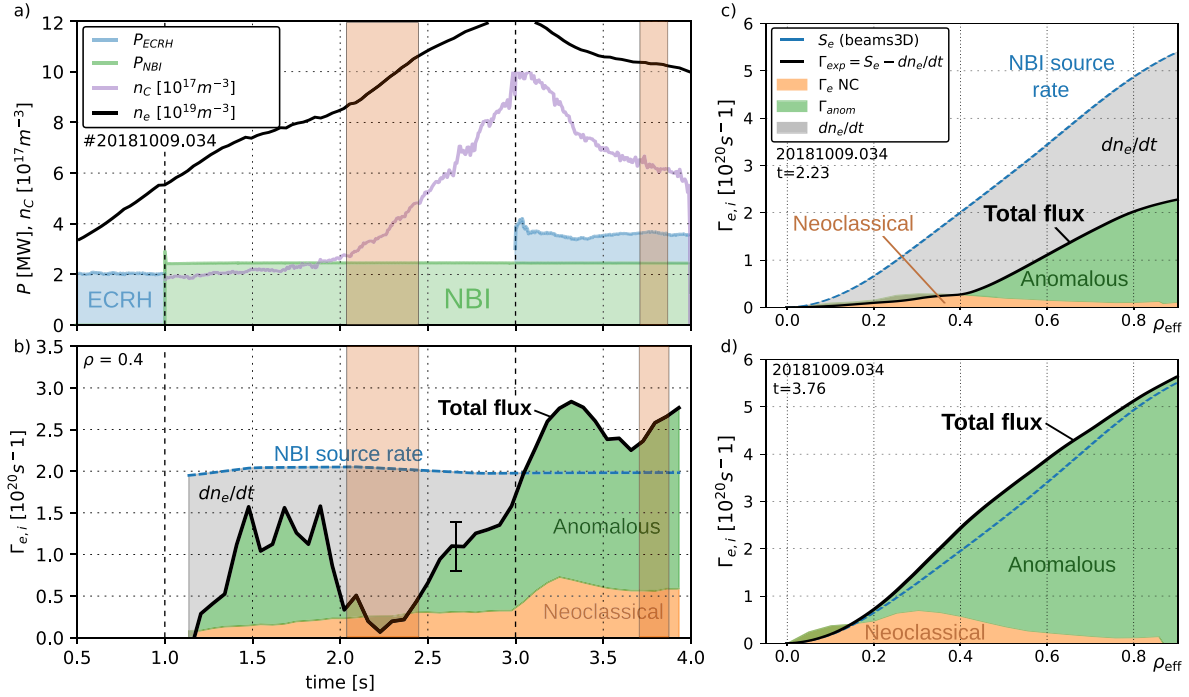
Figure 8. Time trace at $\rho = 0.4$ (*b*) and radial profiles at selected time points (*c*), (*d*) of particle fluxes during NBI/ECRH mixed heating discharge #20181009.034. Experimental fluxes (black) are calculated by subtracting the rate of change of density (shaded gray when positive) from the NBI particle source rate (blue dashed). The difference of experimental and calculated neoclassical (orange) fluxes is attributed to anomalous transport (green). Power and density traces (*a*) from figure 6 are repeated for reference. The profiles are time-averaged over the pure-NBI phase with maximum density rise (*b*) and the mixed NBI+O2 ECRH phase with highest stable performance (*d*), which are highlighted (orange) in the time trace. A representative error bar is shown in (*b*) derived from the average noise level of dn_e/dt.

The dn_e/dt term of equation (1) is calculated from TS data points, normalised to match the line integral provided by the interferometer. The points are binned in time and radius as profile fits either introduce oscillations or limit the spatial resolution below that required to see the inflection point of the density peaking at $\rho = 0.5$, depending on the smoothing strength and fit type chosen. The binning method is more robust and provides less opportunity to influence the result by arbitrarily chosen input parameters. It was necessary in some cases to filter one of the three lasers due to alignment issues that are known to cause strong oscillations in time [59].

Neoclassical particle fluxes Γ_{NC} are calculated with the Neotransp [22] code given profile fits of the main plasma parameters and using tabulated mono-energetic transport coefficients from DKES [23]. It is noted that due to the high density and hence high collisionality reached in the pure-NBI discharges, the classical contribution to the heat and particle fluxes can be significant (20%) and must be included. Despite the high collisionality, the main ions species considered here, including carbon, are not yet in the Pfirsch-Schlüter regime. For heavier ions such as Argon this may be the case and it would be necessary to carefully consider the assumptions of the classical flux calculation. The electric field is calculated according to balance of the ambipolar fluxes and indicates that the full plasma radius is in ion-root in all plasmas presented in this paper. This is confirmed by CXRS measurements of the radial field [60, 61]. The effective charge is assumed

to be $Z_{eff} = 1.2$ in all cases but it was found that a range of $1.1 < Z_{eff} < 1.5$ has only a 30% effect on the calculated fluxes. In the strongest example of impurity peaking included in this work, the effective charge remains below 1.5 as measured by visible Bremsstrahlung [62, 63]. Given the uncertainties due to this and on the input profiles, Γ_{NC} is not used to claim agreement or validation of neoclassical calculations but only to indicate when the anomalous fluxes are clearly dominant.

Figure 8 shows the experimental fluxes and the two terms of equation (1) in comparison to the calculated neoclassical fluxes. The difference is attributed to anomalous transport effects (i.e. turbulence). The noise level of dn_e/dt is the dominant source of random error in the experimental flux and is shown with a single representative error bar as it is relatively constant through time.

Figure 8(*c*) shows the profile at $t = 2.2$ s, just after the onset of the steepest density rise. It can be seen that the experimental flux is at around the same level as the calculated neoclassical flux for $\rho \leqslant 0.4$, indicating the absence or at least very strongly reduction of anomalous fluxes. Since this flux is small compared to the NBI source rate, the density rises rapidly in this region, storing almost all injected particles. Outside this radius the anomalous flux rises almost parallel to the integrated NBI source rate, resulting in only a small density increase in the outer half of the plasma, as seen in the profiles in figure 7. The reason for this sudden spatially localised reduction of anomalous particle transport is currently not understood but
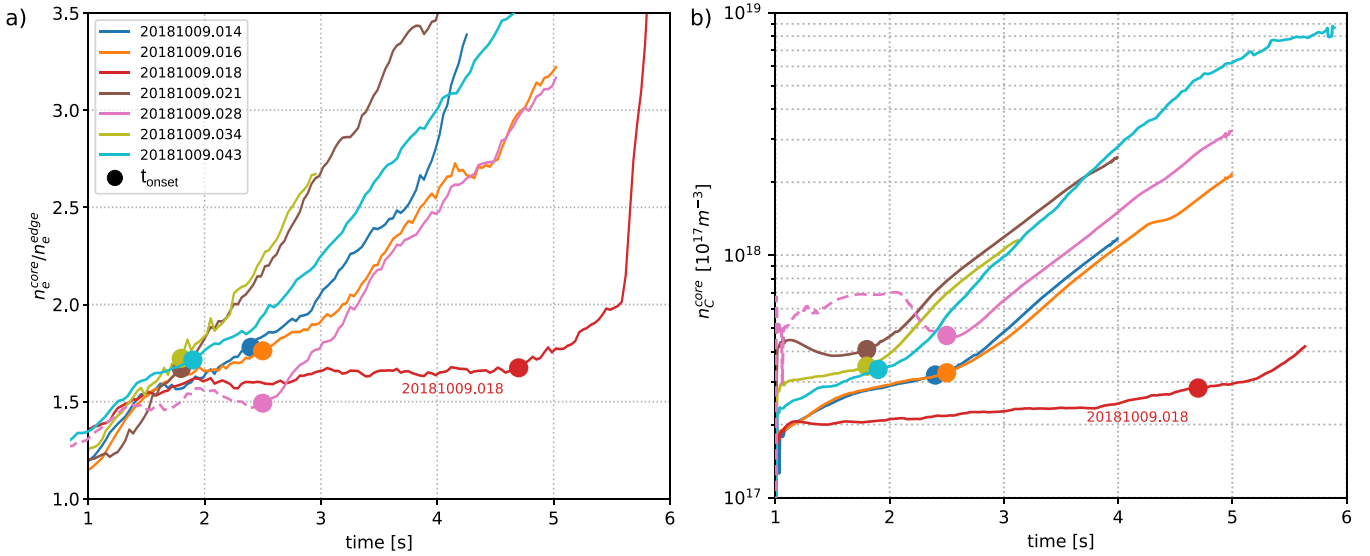
Figure 9. Evolution of electron density peaking factor $n_e^{\text{core}}/n_e^{\text{edge}}$ (*a*) and core carbon density (*b*) during all pure NBI discharges. Approximate 'onset' times are marked by hand.

is clearly the cause of the strong density peaking seen in NBI discharges and occurs in all pure-NBI plasmas, although at different times. It is coincident with a more clearly visible change in the impurity transport and will be discussed more in the next section. Figure 8(*b*) shows that as the density gradient builds, the anomalous particle flux begins to increase again, slowing the core density rise, in this case reaching about 75% of the source rate by $t = 3.0$ s when the O2 ECRH is introduced. With this extra heating, the anomalous flux approximately doubles, rising slightly above the source rate (at $\rho = 0.4$) and ejecting some of the accumulated density, flattening the density profile slightly.

4.2. Impurity transport

The impurity transport in NBI plasmas has been analysed independently [9, 64, 65]. The neoclassical diffusion and convection coefficients calculated by DKES [23]/Neotransp [22] are used with the PySTRAHL [21] impurity transport code to simulate the carbon density profiles and their time dependence. A good match to the measured profile (dashed-green vs C in figure 7(*c*)) is obtained when the anomalous diffusion within $\rho < 0.5$ is reduced to 5% of its value during the ECRH-only phase. In the effective absence of the normally strong anomalous diffusion [24], the pinch of the neoclassical convection is sufficient to drive impurity peaking during the pure-NBI phase. With higher anomalous diffusion values, the observed level of peaking is not reproduced and could only otherwise be explained by adding further anomalous convection. For $\rho > 0.5$ however, anomalous diffusion of $\sim$50% of the ECRH-only level must be maintained to explain the observed shape of the n_C profile, analogous to the main ion fluxes in figure 8(*c*).

To match the time dependence of the central n_C (green in figure 6), the reduction in anomalous diffusion must be made some time after the ECRH-NBI switch over, approximately

coincident with reduction in anomalous flux seen in the main ions.

Figure 9(*b*) shows time traces of the logarithmic core carbon density in all long ($>$2 s) pure NBI discharges in which a clear change in gradient can be seen. This coincides in many cases with a change in the rise rate of the density peaking factor $n_e^{\text{core}}/n_e^{\text{edge}}$, although the change is not as obvious as in the carbon density, and marks the on-set of the reduced particle flux. The time of this change t_{onset}, varies between discharges that have almost the same control waveforms (heating etc). The only significant differences are the gas-puff fuelling and the machine wall condition which modifies the recycling fluxes and hence the initial density level. The discharge #20181009.018 is exceptional in that no gas fuelling is used apart from the initial prefill before breakdown. The discharge begins with very low density and the density and impurity peaking does not begin until the NBI fuelling raises the density to roughly the same level as in the other cases. It is unlikely that the fuelling itself is relevant here, since the behaviour may occur at some critical threshold of a turbulent relevant parameter such as normalised density gradient a/L_n or temperature ratio T_e/T_i that is itself dependent on the fuelling level. That 3.5 s of pure NBI plasma occurs with no significant density or impurity peaking shows clearly that the strong peaking is a consequence of the reduced anomalous transport and not a straightforward result of the NBI core fuelling.

4.3. Heat transport

Analysis of the electron and ion energy fluxes $Q_{\text{i,e}}$ is performed analogous to the particle flux but can in principle be separated for the two species:

$$Q_e(\rho) = \int_0^\rho \left(P_{\text{e}} - P_{\text{ei}} - P_{\text{rad}} - \frac{\text{d}W_e}{\text{d}t} \right) \frac{\text{d}V}{\text{d}\rho'} \, \text{d}\rho' \quad (2)$$
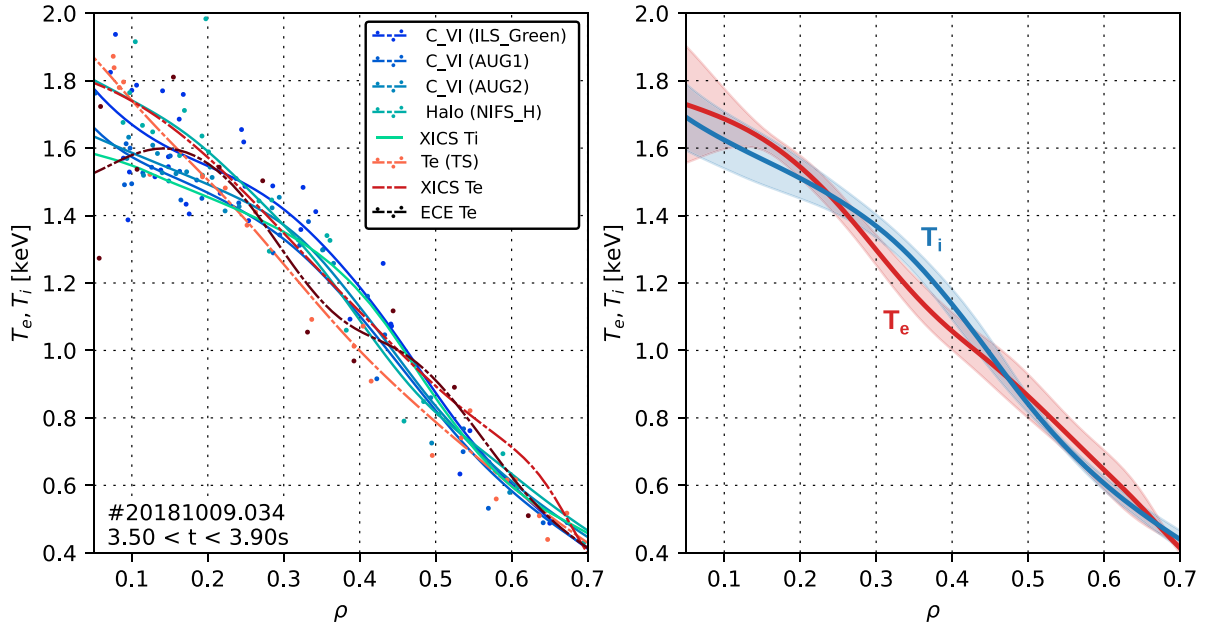
Figure 10. (*a*) Data points and fitted radial profiles from different diagnostics for ion (blue) and electron (red) temperatures during NBI plasma with low power O2 ECRH. (*b*) Average and spread (FWHM) of individual fits as an estimation of systematic errors.

$$Q_{\rm i}\left(\rho\right) = \int_0^\rho \left(P_{\rm i} + P_{\rm ei} - \frac{{\rm d}W_i}{{\rm d}t}\right)\frac{{\rm d}V}{{\rm d}\rho'}\,{\rm d}\rho'. \qquad (3)$$

The electron and ion power deposition profiles $P_{\rm e,i}(\rho')$ are calculated for ECRH using the TRAVIS code [66] and for NBI by Beams3D [52]. The radiated power profile $P_{\rm rad}$ is taken from inversions of bolometry measurements [67] and the stored energy $W(\rho')$ calculated from the electron and ion temperature and density profiles. Power loss due to charge exchange of thermal ions with the edge neutral cloud is neglected as the neutral density is only significant in the outermost part of the plasma ($\rho > 0.8$), as examined in [31]. Consequently, plots are shown only for inside this radius. The collisional electron-ion power transfer term $P_{\rm ei}(\rho')$ is calculated as in [31] as $P_{\rm ei} \propto n_{\rm e}^2 T_{\rm e}^{-3/2}(T_{\rm e} - T_{\rm i})$. The dependence on the temperature difference $\Delta T = T_{\rm e} - T_{\rm i}$ presents a significant measurement challenge, particularly in the high density cases examined here. For example, at $\rho = 0.5$ during the NBI-only phase where $T_{\rm e} = 800\,{\rm eV}$ and $n_e = 7 \times 10^{19}\,{\rm m}^{-3}$, a difference of only $\Delta T = 50\,{\rm eV}$ leads to a power transfer of $P_{\rm ei} \approx 1.3\,{\rm MW}$ which is equal to the full deposited power of the NBI in both species inside that surface. A physically consistent power balance therefore requires $\Delta T < 50\,{\rm eV}$, far below the systematic uncertainties of all $T_{\rm e}$ and $T_{\rm i}$ measurements. The diagnostic data therefore provides effectively no useful information on the individual ion and electron heat fluxes in such plasmas.

In the later phase, the high central ECRH power deposition brings higher $T_{\rm e}$ and hence ΔT, leading to a marginal situation where the diagnostic data might be useful, but its uncertainty assessment is critical. Time averaging of the data over at least 300 ms is required and reduces the statistical uncertainties to effectively negligible, leaving only systematic errors.

Improvements were made to remove known small systematic errors that are often neglected, such as precise determination of the XICS instrument function [68] and correction for fine structure and Zeeman splitting in visible CXRS measurements using a fully resolved spectral model [69]. The remaining systematic uncertainties are difficult to quantify since the causes are unknown. For an indication of the systematic uncertainty, the differences between alternate diagnostics providing the same quantity can be examined. Figure 10(*a*) shows data and fitted profiles of $T_{\rm e}$ from TS, the x-ray imaging crystal spectrometer (XICS) [33], electron cyclotron emission (ECE) [70] and $T_{\rm i}$ from XICS as well as different species and spectrometers of the CXRS system. For XICS $T_{\rm e}$ and $T_{\rm i}$, no data points can be shown as profiles must be inverted from line-integrated measurements [71]. These inverted profiles have an offset of -200 eV applied, as determined from a campaign-wide database comparison with CXRS measurements. ECE measurement positions are calculated with a single iteration of the TRAVIS [66] radiation transport code and only the low field side is shown as the core density is close to cut-off. Figure 10(*b*) shows the average of the fits for electrons and ions, with error bands derived from the spread of fits of the different sources.

Figure 11 shows electron and ion energy fluxes as calculated from equations (2) and (3) in comparison to the neoclassical energy fluxes calculated from Neotransp. The uncertainty band represents the spread of energy fluxes (full-width at half maximum) due to the $P_{\rm ei}$ values from the various diagnostic combinations for $T_{\rm e}$ and $T_{\rm i}$. The small $T_{\rm e}$—$T_{\rm i}$ difference leads to a large ion heat flux uncertainty covering a range from $Q_{\rm i} = 0$ to higher than the deposited power $Q_{\rm i} > P_{\rm i}$, i.e. indicating that it is possible for some power to be transferred from electrons to ions. A reduction of the ion heat
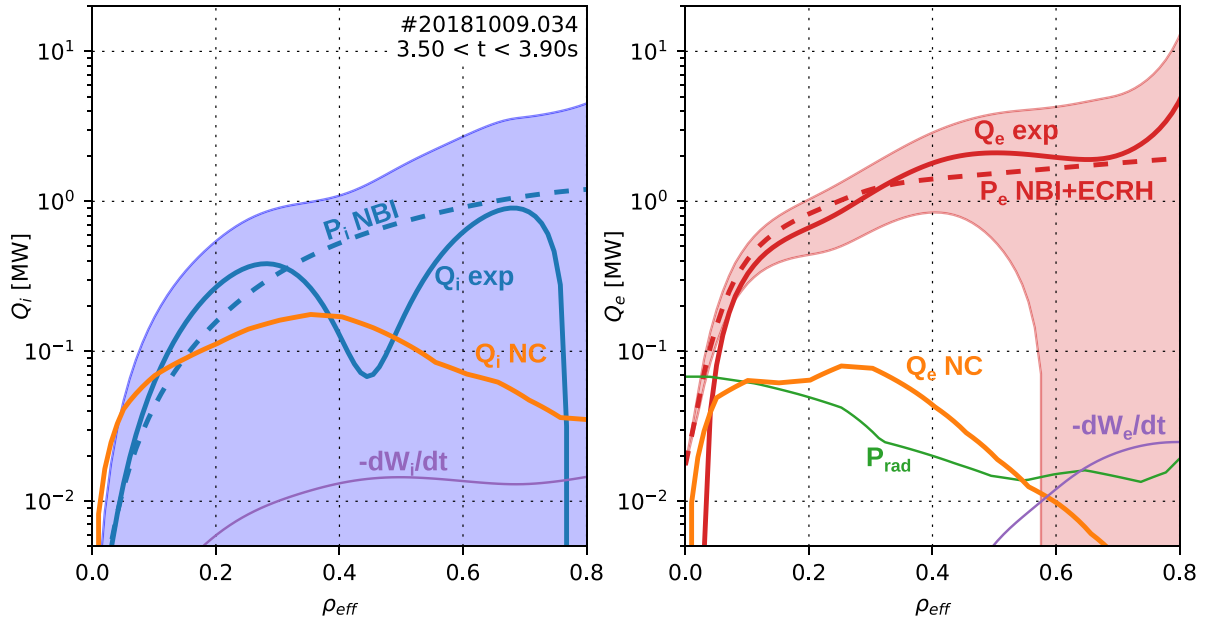
Figure 11. (*a*) Ion and (*b*) electron power balance profiles. Experimental fluxes (solid red/blue, with uncertainty band) compared to calculated neoclassical fluxes (orange). Components of the experimental fluxes are also shown: ECRH+NBI power deposition (dashed red/blue), change of stored energy (purple) and radiation (green). The uncertainty band represents the range of T_e and T_i measurements.

transport to neoclassical levels at around $\rho \sim 0.5$ is suggested by the averaged diagnostic data and this would fit well with both the particle and impurity transport picture as well as the strong reduction of ion heat flux seen in the post-pellet high-performance discharges [7]. However, since there is no fundamental reason to assume that the systematic errors should average out, this is not conclusive without a more careful analysis and experiments with higher quality measurements in subsequent campaigns. The electron heat flux on the other hand is clearly strongly anomalous and the temperature profiles that would be required to indicate fully neoclassical electron heat flux are well outside the uncertainty of the diagnostic data. It should be noted that a reduction in the heat transport of one species (e.g. ions), while interesting, is of limited use for developing high-performance scenarios at high collisionality since the energy transport of that species is immediately dominated by transport via the other species.

From a scenario development perspective, it is therefore more useful to examine the total heat transport, where the P_{ei} term is not required:

$$Q_{\text{tot}} = \int_0^\rho \left(P_e + P_i - P_{\text{rad}} - \frac{dW}{dt} \right) \frac{dV}{d\rho'} \, d\rho' \qquad (4)$$

Figure 12 shows the total energy flux profiles during the pure-NBI and NBI+ECRH phases as well as the time trace of total energy flux near mid-radius. The total fluxes are dominated by anomalous fluxes at all times and all radii outside the very centre ($\rho > 0.2$). This is the case for all such discharges except when the pure-NBI phase continues for 5 s and impurity accumulation leads to strong radiation from the core, which dominates the power loss inside $\rho \sim 0.3$. Most interestingly, no significant change in the total heat transport is seen at the

onset time when the particle and impurity transport changes abruptly. As discussed, it remains possible that the ion heat transport channel is effected but the total is dominated by the electrons. While the separation of the channels is of little use for scenario development, it would provide useful information on which turbulent mechanisms are responsible for each channel if one can be shown to have similar behaviour as the particle transport.

Figure 12(*b*) shows a significant increase in the anomalous heat flux during the NBI+ECRH phase. The scaling of the anomalous transport can be assessed by examining the relationship between temperature gradient and anomalous heat flux for a variety of plasmas. This is done at mid-radius to avoid the vanishingly small heat flux and temperature gradient near the plasma core and inaccuracy due to the neglect of charge-exchange losses near the plasma edge. For a simple effective heat diffusivity of χ for both electrons and ions of equal temperature, the expected relationship would be $Q_{\text{tot}} = 2n_e \chi \nabla T$. Figure 13(*a*) shows all time points from several discharges involving NBI heating in which most points show a relationship of anomalous heat flux broadly consistent with a heat diffusivity of around $\chi = 0.25 \pm 0.1 \, \text{m}^2 \, \text{s}^{-1}$. The exceptional points (A) are plasmas with high ECRH power where heat diffusivity is far higher with $\chi \sim 1$, broadly consistent with the ITG-dominated pure ECRH discharges examined in [31](reproduced here in gray). Plasmas with only NBI heating (B) have a significantly improved heat diffusivity and achieve similar temperature gradients and core T_i despite significantly lower energy flux. Most interestingly, plasmas with mild additional ECRH heating (C) maintain the low heat diffusivity and obtain significantly higher temperature gradients. Figure 13(*b*) shows the same plasmas in the space of normalised ion temperature and density gradients in which the plasmas with low
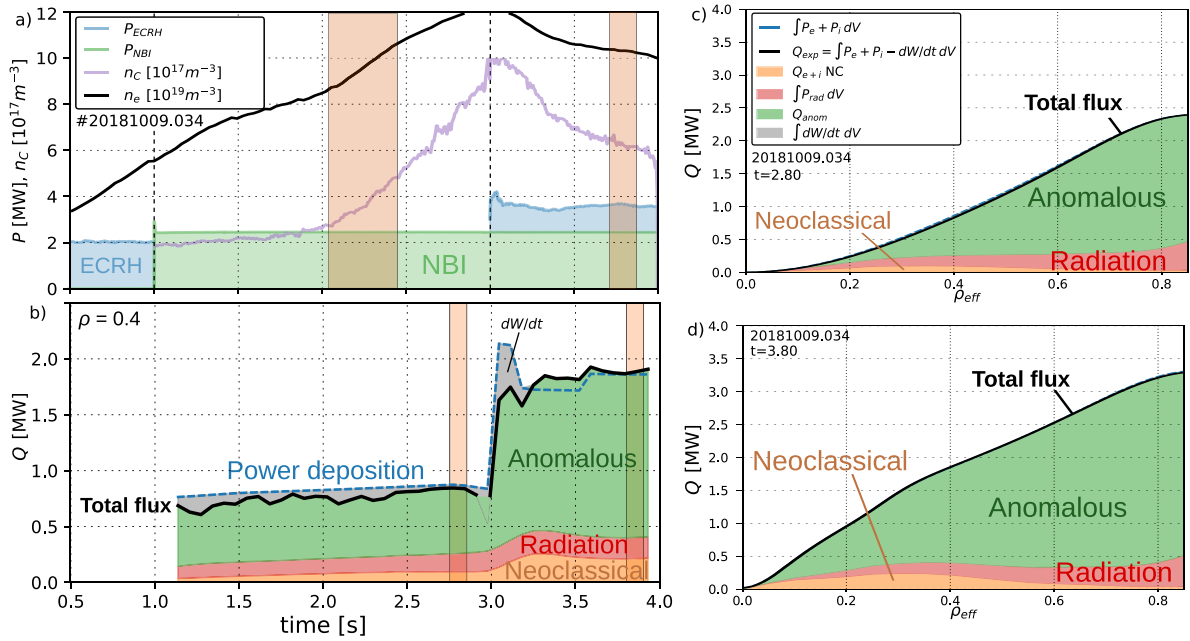
Figure 12. Time trace for $\rho = 0.4$ (*b*) and radial profiles at selected time points (*c*), (*d*) of energy fluxes during NBI/ECRH mixed heating discharge #20181009.034. Experimental fluxes (black) are calculated by subtracting the rate of stored energy (shaded gray when +ve) from the NBI and ECRH deposited power (blue dashed). The difference between experimental and calculated neoclassical (orange) and measured radiation (red) fluxes is attributed to anomalous transport (green). Power and density traces (*a*) from figure 6 are repeated for reference. The profiles are time-averaged over the end of the pure-NBI phase (*c*) and the mixed NBI+O2 ECRH phase with stable performance (*d*), which are highlighted (orange) in the time trace.
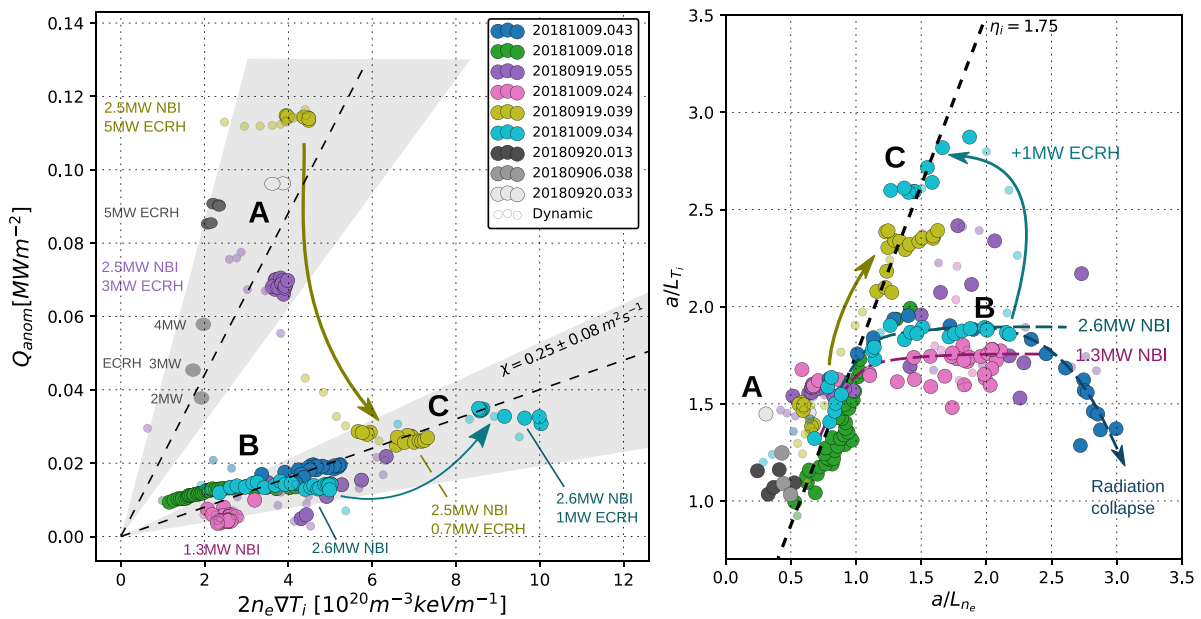
Figure 13. Left: anomalous heat flux versus $2n_e \nabla T_i$ and right: normalised ion temperature gradient versus electron density gradient for a selection of shots involving mixed heating scenarios. Three groups of plasmas are indicated: (*A*) High ECRH power (>2 MW) plasmas with high ion heat flux but low achieved temperature gradients, (*B*) Pure NBI plasmas with high density gradient and low heat diffusivity but low total heat flux and hence low ion temperature gradient, (*C*) NBI plasmas with high density gradient and low (<2 MW) but sufficient ECRH power to achieve higher temperature gradients. Left is shown a line of constant heat diffusivity $Q_{anom} = \chi 2n_e \nabla T_i$ with $\chi \approx 0.25$ and right is shown a line of constant $\eta_i = L_{T_i}/L_{n_e}$.

heat diffusivity show significantly higher density gradients (B and C). In pure-NBI discharges (B), the density gradient builds up while a/L_{T_i} saturates due to reducing power per particle as the density increases. Eventually, the density rise and impurity accumulation lead to a reduction of the energy flux and hence a/L_{T_i} due to strong core Bremsstrahlung radiation, as
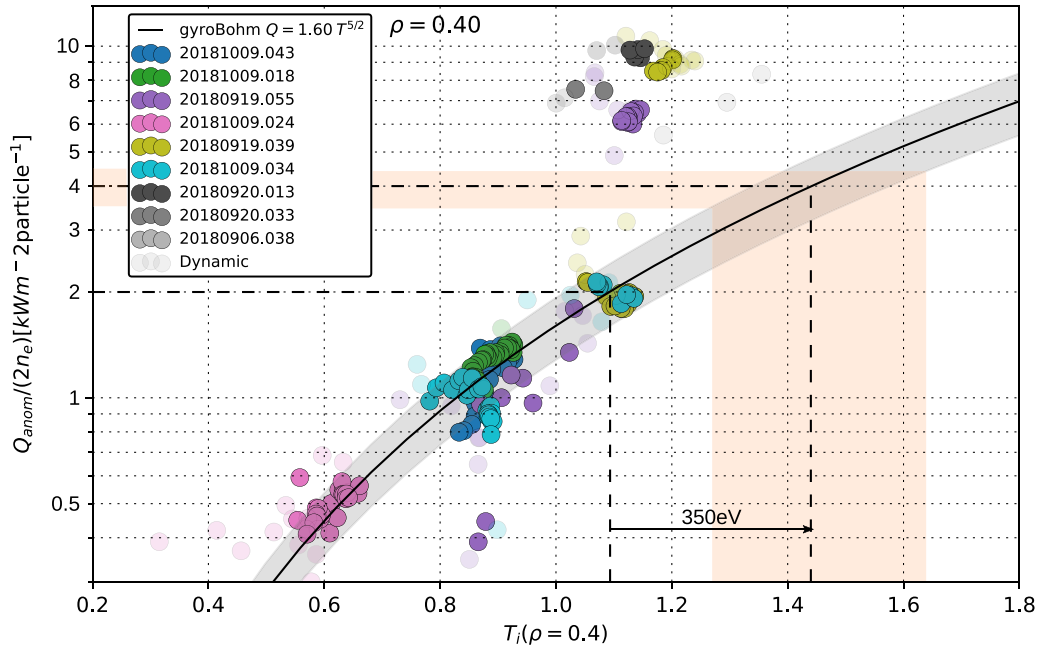
Figure 14. Energy flux per particle versus ion temperature in the steep gradient region for a selection of shots involving mixed heating scenarios. Also plotted is gyro-Bohm scaling $Q \propto n_e T^{5/2}$ with fitted scaling factor and the projection of possible T_i at mid-radius based on a doubling of the NBI and ECRH power compared to the highest T_i discharges measured so far.

in #20181009.043 (dark blue). The highest performance in #20181009.034 (light blue) is achieved by reintroduction of O2 ECRH before the impurity accumulation becomes significant, providing the necessary power to raise the temperature gradients significantly (blue arrow) while the heat diffusivity remains at the reduced level of $\chi = 0.25\,\mathrm{m}^2\,\mathrm{s}^{-1}$. In #20180919.055 (yellow), the same scenario is achieved in a different way, starting from an ECRH ITG dominated plasma with high heat diffusivity and low density gradient. The ECRH power is reduced to 0.7 MW, after which the density gradient begins to rise and with it the temperatures, giving the same final heat diffusivity as the other cases (yellow arrow).

It is clear from both the global performance (figure 5) and the local heat diffusivity (figure 13) that turbulence is significantly reduced in scenarios with lower ECRH power, coincident with the steeper density gradients. This is supported by measurements of turbulent fluctuations with the Doppler reflectometer [34] and phase contrast imaging [72, 73] diagnostics. A deeper discussion of the turbulence mechanisms and their suppression is presented in [34], where it is argued that the reduced turbulence is directly attributable to the density gradients, or more specifically the ITG-driving gradient ratio $\eta_i = L_n/L_{T_i}$. Higher electron temperatures in ECRH heated discharges may also play a role but are clearly not the most significant effect given that the two clouds of data for discharge 20181009.034 have a range of $0.9 < T_e < 1.7$ and all show $\chi \approx 0.25\,\mathrm{m}^2\,\mathrm{s}^{-1}$, whereas discharge 20180920.033 has $T_e = 2.5\,\mathrm{keV}$ with four times greater heat diffusivity.

Unlike the main ion particle and impurity transport, the total heat flux never approach neoclassical values, indicating that at least one type of turbulence is still dominant in at least

the electron energy channel. The total heat flux of the turbulence reduced cases appears to exhibit a simple gyro-Bohm like scaling with the local temperatures in the gradient region $Q \propto n_e T^{5/2}$ (In these cases $T_e \approx T_i$), as suggested by turbulent transport models in Tokamaks [74, 75]. This is shown in figure 14, where all low ECRH power points follow well a gyro-Bohm-like scaling while the high power cases are significantly above, reflecting the dramatic increase in the turbulent heat flux with flatter density gradients. This scaling give a first indication of what might be achieved in W7-X with future increases of heating power. For example, if the gyro-Bohm scaling is maintained with a doubling of the heat flux, a $350 \pm 100\,\mathrm{eV}$ increase of T_i would be expected at this location ($\rho = 0.4$).

4.4. Scaling to higher input power

In the next campaign, two additional NBI sources will be available, doubling both the NBI heating power and particle source rate and in the further future, an upgrade to 8 sources is considered. It is therefore useful to examine what performance, in particular of ion temperature, might be achieved with increased power in these scenarios. In general, such predictions are necessarily very speculative because the particle transport is poorly understood and it has been clearly seen that the heat transport depends strongly on the density profile gradients. However, some simple assumptions can be made to determine the best- and worst-case scenarios.

The first case to consider is one in which the increased NBI particle fuelling leads to a proportional increase in the core density. With NBI alone, this gives no significant increase
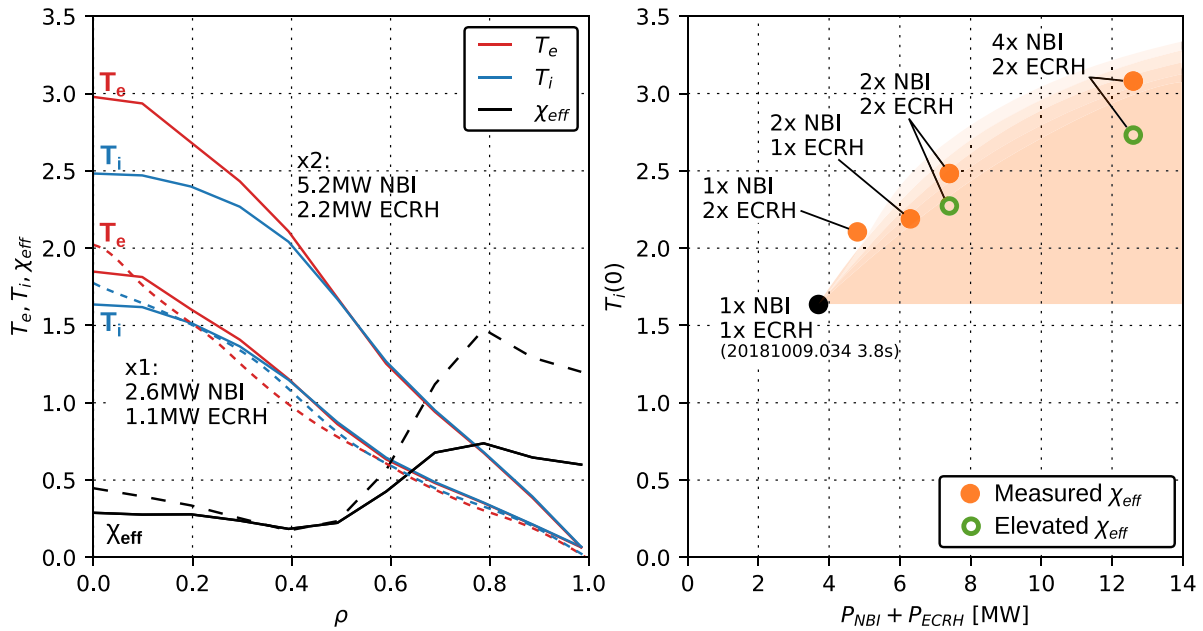
Figure 15. Results of NTSS transport simulations at constant anomalous heat diffusivity and density. (*a*) Electron (red) and ion (blue) temperature profiles from simulations based on the heat diffusivity profile (solid black) determined from steady state phase of discharge 20181009.034 with 2.6 MW of NBI and 1.1 MW of ECRH. Lower profiles show the simulation matched to the original discharge (dashed blue/red) and upper profiles show a doubling of both NBI and ECRH power deposition profiles. (*b*) Central ion temperature for original (black) and for different combinations of ECRH and NBI power scaling (orange points) with respect to the original discharge. Green points show two simulations assuming increased anomalous transport outside of the steep density gradient region (dashed χ in (*a*)). Orange shaded region shows the range of possible values from these simulations through to the ITG dominated scenario, depending on particle transport.

in T_i, since the power per particle remains the same. Strong impurity accumulation will then lead to strong core radiation and reducing temperatures. These might be mitigated by additional ECRH power, but the precise behaviour of the density profile response to the ECRH power is unknown. In the worst case, a further increase over that used in #20181009.034 will completely flatten the density profile, returning to plasmas with clamped $T_i \approx 1.6$ keV. A more favourable assumption would be a reduction of the core density proportionally to the level of ECRH power used, in which case a carefully balanced increase of NBI and ECRH powers could be used to achieve the density profile desired. This represents the best case scenario for T_i, since both powers can be increased with the same density profile. Assuming that the same density profile allows the same heat diffusivity, it is possible to model effect of the increased heat flux. Transport simulations with the NTSS code were conducted based on the anomalous heat diffusivity profile obtained from the steady-state phase of the highest T_i in the NBI+ECRH plasma #20181009.034.

The simulation is first used to reproduce the experimental temperature profiles at the NBI and ECRH powers used in the experiment and then at integer multiples of these. While the anomalous heat diffusivity is fixed at the experimental values, the neoclassical transport is calculated self consistently with the simulated temperature profiles. Changes to the NBI electron and ion power deposition profiles due to changes in the collisionality of the NBI fast ions with each species are not currently taken into account and power depositions profiles are simply scaled by constant factors. However, since the density profile is assumed to remain the same, a large change in collisionality is not expected.

Figure 15(*a*) shows the anomalous heat diffusivity profile determined from the 2.6 MW NBI (2 sources) + 1.1 MW ECRH experiment (solid black) from the 2018 campaign (#20181009.034), as well as the simulated temperature profiles for a doubling of both the NBI and ECRH power that will be attempted in the next campaign (4 sources, 2.2 MW ECRH), assuming the same density profile. Figure 15(*b*) shows the prediction for $T_i(\rho = 0)$ in these cases (orange) as well as in the case of four times the NBI power (8 sources) that is a possible future upgrade of W7-X. The worse case scenario is that in which the additional NBI power would have the same effect on the density profile as higher ECRH powers have shown, limiting the density gradient and returning to strongly turbulent plasmas with clamped T_i. In that case, the ion temperature would remain around this level almost regardless of additional heating power from either system. The two cases give the range of ion temperature that might be achieved in future mixed NBI-ECRH plasmas if no dramatic changes in particle or energy transport behaviour occurs. With 8 NBI sources, the maximum ion temperature lies in the range $1.6 < T_i < 3.0$ keV (figure 15, orange shaded area).

Other assumptions about the details of the heat or particle transport lead to predictions between these two extremes. For example, given that the reduced turbulence is generally coincident with the high density gradient region, and that the particle and impurity transport in the NBI discharges show still strong turbulence outside of mid-radius, it is reasonable to expect that the outer part of the profile shows the strong turbulent scaling and therefore a significant increase in the heat diffusivity. The green points in figure 15 show a more conservative prediction, where the edge heat diffusivity is increased

such that the temperatures profiles remain the same up to $\rho = 0.6$ (i.e. 'clamped' behaviour). The diffusivity in the very core is also slightly increased to reflect the expected strong dependence of ITG turbulence drive on T_e/T_i ratio [31], which is slightly elevated due to the higher ECRH power.

Another assumption would be that the strong turbulence regime shows a dependence on η_i, rather than directly on a/Ln_e. In this case, a steeper density gradient is required to maintain the observed heat diffusivity at higher temperature gradients. This gives reduced heat per particle and therefore also lower T_i than the most optimistic case calculated above.

5. Discussion and outlook

Several scenarios with evidence of reduced turbulent energy transport have been presented which appear to be a result of strong density gradients. While the mechanism behind this link is of interest for turbulence studies, the most important questions for high-performance scenario development are its quantitative relationship and most critically how such density gradients can be created, maintained and controlled. The strongest gradients and hence highest performances have resulted from a rapid injection of hydrogen pellets, but these may be difficult to maintain in steady-state. Low-power discharges after boronisation show good steady-state performance but may not scale to high power. Pure NBI discharges show strong density gradients and reduced heat diffusivity but lack the power per particle required to take advantage of this and also suffer from strong impurity accumulation. The addition of low ECRH power allows control of the impurity accumulation while the heat diffusivity remains low, achieving relative performance above that of plasmas with high ECRH power. However, the additional ECRH reduces the density peaking slightly and it is not clear at what ECRH power level the density gradient is reduced to a level such that strong turbulent transport returns. Neither the mechanism behind the reduction of the density gradient with ECRH, nor the apparent spontaneous appearance of it in pure NBI experiments is currently understood and study of the anomalous particle transport, particularly in relation to ECRH power deposition, is arguably the most important next step for the development of high-performance scenarios at W7-X. Nethertheless, given the data observed so far, a careful balance of ECRH and NBI power provides one of the most promising routes to steady-state high-performance scenarios in W7-X, particularly with high T_i.

The subsequent campaign of W7-X begun in 2022 and offered the opportunity to further explore these scenarios. Alongside deeper studies of the relationship of turbulent fluctuations and heat flux with density gradients, a strong focus of the experimental program was on the density profile and its control. The NBI+ECRH scenario was revisited to examine the value and abruptness of the threshold in ECRH power that leads to loss of the density profile gradients and the associated higher turbulence. Detailed transport analysis is not yet complete, but it already evident that an optimum level of ECRH power below this threshold could be found that maintained

a higher central T_i with the existing heating systems, located around the first orange point in figure 15.

A range of possibilities for development of turbulence reduced scenarios exist and it should be possible to raise T_i to values approaching those seen for the pellets discharges, but in timescales far longer than the energy confinement times and limited only by the operational limits of the NBI heating system(~ 10 s). The heat transport of W7-X is now relatively well characterised empirically and most of all has been shown to depend heavily on the density gradients and hence the particle transport. Meanwhile, the particle transport itself is very poorly understood. Furthermore, the particle transport appears to exhibit threshold-like behaviour and so affects heat transport in a way that small changes in input power can dramatically change the achieved performance. Only with a detailed understanding of those thresholds and the underlying mechanism gained in the next experimental campaigns, will a reliable scaling of the performance of W7-X to a reactor be possible.

ORCID iDs

O.P. Ford https://orcid.org/0000-0002-5646-4758
M. Beurskens https://orcid.org/0000-0002-3354-0279
S.A. Bozhenkov https://orcid.org/0000-0003-4289-3532
S. Lazerson https://orcid.org/0000-0001-8002-0121
A. Alonso https://orcid.org/0000-0001-6863-8578
J. Baldzuhn https://orcid.org/0000-0001-5667-351X
G. Fuchert https://orcid.org/0000-0002-6640-2139
D. Hartmann https://orcid.org/0000-0002-3511-6500
A. Langenberg https://orcid.org/0000-0002-2107-5488
N. Pablant https://orcid.org/0000-0001-6617-8459
F. Reimold https://orcid.org/0000-0003-4251-7924
T. Romba https://orcid.org/0000-0002-2727-9385
T. Stange https://orcid.org/0000-0003-4154-1455
D. Gradic https://orcid.org/0000-0002-6109-9345
R.C. Wolf https://orcid.org/0000-0002-2606-5289
D. Zhang https://orcid.org/0000-0002-5800-4907

References

[1] Pedersen T. *et al* 2017 Key results from the first plasma operation phase and outlook for future performance in Wendelstein 7-X *Phys. Plasmas* **24** 055503
[2] Wolf R. *et al* 2017 Major results from the first plasma campaign of the Wendelstein 7-X stellarator *Nucl. Fusion* **57** 102020

[3] Klinger T. *et al* 2019 Overview of first Wendelstein 7-X high-performance operation *Nucl. Fusion* **59** 112004

[4] Wolf R.C. *et al* 2018 Electron-cyclotron-resonance heating in Wendelstein 7-X: a versatile heating and current-drive method and a tool for in-depth physics studies *Plasma Phys. Control. Fusion* **61** 014037

[5] Endler M. *et al* 2021 Wendelstein 7-X on the path to long-pulse high-performance operation *Fusion Eng. Des.* **167** 112381

[6] Laqua H. *et al* (The W7-X Team) 2021 High-performance ECRH at W7-X: experience and perspectives *Nucl. Fusion* **61** 106005

[7] Bozhenkov S. *et al* 2020 High-performance plasmas after pellet injections in Wendelstein 7-X *Nucl. Fusion* **60** 066011

[8] Beidler C. *et al* 2021 Demonstration of reduced neoclassical energy transport in Wendelstein 7-X *Nature* **596** 221–6

[9] Vanó L. 2022 Carbon content and transport investigations on Wendelstein 7-X with charge exchange recombination spectroscopy *PhD Thesis* TU/e Berlin (available at: https://depositonce.tu-berlin.de/items/f56d13a8-ffa5-4d64-bb2a-67a446d8f80e)

[10] Winters V. 2019 Carbon sourcing and transport in the island divertor of Wendelstein 7-X *PhD Thesis* University of Wisconsin-Madison (available at: https://search.library.wisc.edu/catalog/9912890869902121)

[11] Sereda S. *et al* 2020 Impact of boronizations on impurity sources and performance in Wendelstein 7-X *Nucl. Fusion* **60** 086007

[12] Bozhenkov S. *et al* 2017 The thomson scattering diagnostic at Wendelstein 7-X and its performance in the first operation phase *J. Instrum.* **12** P10004

[13] Brunner K., Akiyama T., Hirsch M., Knauer J., Kornejew P., Kursinski B., Laqua H., Meineke J., Mora H.T. and Wolf R.C. 2018 Real-time dispersion interferometry for density feedback in fusion devices *J. Instrum.* **13** P09002

[14] Knauer J. *et al* 2016 A new dispersion interferometer for the stellarator Wendelstein 7-X *Proc. 43rd EPS Conf. on Plasma Physics* (*Leuven, Belgium, 4–8 July 2016*) p P4.017 (available at: http://ocs.ciemat.es/EPS2016PAP/pdf/P4.017.pdf)

[15] Ford O.P. *et al* 2020 Charge exchange recombination spectroscopy at Wendelstein 7-X *Rev. Sci. Instrum.* **91** 023507

[16] Romba T. 2021 Validation of the W7-X CXRS for impurity density profiles *Master's Thesis* TU/e Eindhoven (available at: https://research.tue.nl/nl/studentTheses/validation-of-the-W7-X-cxrs-for-impurity-density-profiles)

[17] Beidler C.D., Feng Y., Geiger J., Köchl F., Maßberg H., Marushchenko N.B., Nührenberg C., Smith H.M. and Turkin Y. 2018 (Expected difficulties with) density-profile control in W7-X high-performance plasmas *Plasma Phys. Control. Fusion* **60** 105008

[18] Maaßberg H., Beidler C.D. and Simmet E.E. 1999 Density control problems in large stellarators with neoclassical transport *Plasma Phys. Control. Fusion* **41** 1135–53

[19] Turkin Y., Beidler C.D., Maaßberg H., Murakami S., Tribaldos V. and Wakasa A. 2011 Neoclassical transport simulations for stellarators *Phys. Plasmas* **18** 022505

[20] Burhenn R. *et al* 2009 On impurity handling in high performance stellarator/heliotron plasmas *Nucl. Fusion* **49** 065005

[21] Swee C., Geiger B., Dux R., Kumar S.T.A., Castillo J.F., Bader A. and Gerard M. 2021 Impurity transport studies at the HSX stellarator using active and passive CVI spectroscopy *Plasma Phys. Control. Fusion* **64** 015008

[22] Smith H. 2021 NEOTRANSP: Tools for neoclassical transport calculations (available at: https://gitlab.mpcdf.mpg.de/smithh/neotransp)

[23] van Rij W.I. and Hirshman S.P. 1989 Variational bounds for transport coefficients in three-dimensional toroidal plasmas *Phys. Fluids* B **1** 563–9

[24] Geiger B. *et al* 2019 Observation of anomalous impurity transport during low-density experiments in W7-X with laser blow-off injections of iron *Nucl. Fusion* **59** 046009

[25] Swee C., Geiger B., Ford O., Nornberg M.D., O'Mullane M., Poloskei P.Z., Reimold F., Romba T. and Wegner T. 2024 Impurity transport study based on measurement of visible wavelength high-n charge exchange transitions at W7-X *Nucl. Fusion* **64** 086062

[26] Langenberg A. *et al* 2020 Charge-state independent anomalous transport for a wide range of different impurity species observed at Wendelstein 7-X *Phys. Plasmas* **27** 052510

[27] Winters V.R. *et al* 2021 EMC3-EIRENE simulation of first wall recycling fluxes in W7-X with relation to H-alpha measurements *Plasma Phys. Control. Fusion* **63** 045016

[28] Kremeyer T. *et al* (The W7-X Team) 2022 Analysis of hydrogen fueling, recycling and confinement at Wendelstein 7-X via a single-reservoir particle balance *Nucl. Fusion* **62** 036023

[29] Stroth U., Geist T., Koponen J.P.T., Hartfuß H.-J. and Zeiler P. (ECRH and W7-AS Team) 1999 Evidence for convective inward particle transport in a stellarator *Phys. Rev. Lett.* **82** 928–31

[30] Hirsch M. *et al* 2008 Major results from the stellarator Wendelstein 7-AS *Plasma Phys. Control. Fusion* **50** 053001

[31] Beurskens M. *et al* (The W7-X Team) 2021 Ion temperature clamping in Wendelstein 7-X electron cyclotron heated plasmas *Nucl. Fusion* **61** 116072

[32] Beurskens M. *et al* (The W7-X Team, The ASDEX Upgrade Team and The EUROfusion MST1 Team) 2021 Confinement in electron heated plasmas in Wendelstein 7-X and ASDEX Upgrade; the necessity to control turbulent transport *Nucl. Fusion* **62** 016015

[33] Langenberg A. *et al* 2018 Prospects of x-ray imaging spectrometers for impurity transport: recent results from the stellarator Wendelstein 7-X *Rev. Sci. Instrum.* **89** 10G101

[34] Carralero D. *et al* 2021 An experimental characterization of core turbulence regimes in Wendelstein 7-X *Nucl. Fusion* **61** 096015

[35] Bähner J.-P. *et al* 2021 Phase contrast imaging measurements and numerical simulations of turbulent density fluctuations in gas-fuelled ECRH discharges in Wendelstein 7-X *J. Plasma Phys.* **87** 905870314

[36] Yamada H. *et al* 2005 Characterization of energy confinement in net-current free plasmas using the extended international stellarator database *Nucl. Fusion* **45** 1684–93

[37] Warmer F. *et al* 2021 Impact of magnetic field configuration on heat transport in stellarators and heliotrons *Phys. Rev. Lett.* **127** 225001

[38] Baldzuhn J. *et al* 2020 Enhanced energy confinement after series of pellets in Wendelstein 7-X *Plasma Phys. Control. Fusion* **62** 055012

[39] Xanthopoulos P. *et al* 2020 Turbulence mechanisms of enhanced performance stellarator plasmas *Phys. Rev. Lett.* **125** 075001

[40] Proll J.H.E., Helander P., Connor J.W. and Plunk G.G. 2012 Resilience of quasi-isodynamic stellarators against trapped-particle instabilities *Phys. Rev. Lett.* **108** 245002

[41] Alcusón J., Xanthopoulos P., Plunk G.G., Helander P., Wilms F., Turkin Y., Stechow A.V. and Grulke O. 2019 Suppression of electrostatic micro-instabilities in maximum-J stellarators *Plasma Phys. Control. Fusion* **62** 035005

[42] Estrada T. *et al* (The W7-X Team) 2021 Radial electric field and density fluctuations measured by Doppler reflectometry during the post-pellet enhanced confinement phase in W7-X *Nucl. Fusion* **61** 046008

[43] Stechow A.V. *et al* 2020 Suppression of core turbulence by profile shaping in Wendelstein 7-X (arXiv:2010.02160)

[44] Langenberg A. *et al* (The W7-X Team) 2021 Impurity transport in ion- and electron-root confinement scenarios at Wendelstein 7-X *Nucl. Fusion* **61** 116018

[45] Warmer F., Beidler C.D., Dinklage A. and Wolf R. 2016 From W7-X to a HELIAS fusion power plant: motivation and options for an intermediate-step burning-plasma stellarator *Plasma Phys. Control. Fusion* **58** 074006

[46] Meitner S.J., Baylor L.R., Gebhart T.E., Harris J.H., Mcginnis W.D., Bjorholm T.P. and Logan K.G. 2020 Design of a continuous pellet fueling system for Wendelstein 7-X *IEEE Trans. Plasma Sci.* **48** 1585–90

[47] Zhang D. *et al* 2023 Observation of impurity accumulation and its compatibility with high plasma performance in W7-X *Plasma Phys. Control. Fusion* **65** 105006

[48] Lunsford R. *et al* 2021 Characterization of injection and confinement improvement through impurity induced profile modifications on the Wendelstein 7-X stellarator *Phys. Plasmas* **28** 082506

[49] McNeely P. *et al* 2019 Commissioning and initial operation of the W7-X neutral beam injection heating system *Fusion Eng. Des.* **161** 111997

[50] Lazerson S.A. *et al* (The W7-X Team) 2021 First neutral beam experiments on Wendelstein 7-X *Nucl. Fusion* **61** 096008

[51] Spanier A. *et al* 2021 Performance of the first neutral beam injector at the Wendelstein 7-X stellarator *Fusion Eng. Des.* **163** 112115

[52] Lazerson S.A. *et al* (The W7-X Team) 2021 Modeling and measurement of energetic particle slowing down in Wendelstein 7-X *Nucl. Fusion* **61** 096005

[53] Gradic D., Dinklage A., Brakel R., McNeely P., Osakabe M., Rust N. and Wolf R. 2015 Assessment of the plasma start-up in Wendelstein 7-X with neutral beam injection *Nucl. Fusion* **55** 033002

[54] Lazerson S.A. *et al* 2020 Validation of the BEAMS3D neutral beam deposition model on Wendelstein 7-X *Nucl. Fusion* **60** 076020

[55] Fujii K., Goto M. and Morita S. 2015 Study of neutral hydrogen transport in LHD core plasmas based on high dynamic-range Balmer-α spectroscopy *Nucl. Fusion* **55** 063029

[56] Poloskei P.Z., Geiger B., Jansen van Vuuren A., Äkäslompolo S., Ford O.P., Spanier A., Neelis T.W.C., McNeely P. and Hartmann D. 2023 Experimental characterization of the active and passive fast-ion H-alpha emission in W7-X using FIDASIM *Nucl. Fusion* **64** 026008

[57] McMillan M. and Lazerson S.A. 2014 BEAMS3D neutral beam injection model *Plasma Phys. Control. Fusion* **56** 095019

[58] Bannmann S. *et al* 2022 Modeling the beam emission Balmer-α spectrum in neutral beam heated plasmas at Wendelstein 7-X *Proc. 2022 DPG Spring Meeting* (*Mainz, Germany*, *28 March–1 April 2022*) p P4.017 (available at: https://mainz22.dpg-tagungen.de)

[59] Fuchert G., Nelde P., Pasch E., Beurskens M.N.A., Bozhenkov S.A., Brunner K.J., Meineke J., Scott E.R. and Wolf R.C. 2022 A novel technique for an alignment-insensitive density calibration of Thomson scattering diagnostics developed at W7-X *J. Instrum.* **17** C03012

[60] Alonso J. *et al* (The W7-X Team) 2022 Plasma flow measurements based on charge exchange recombination spectroscopy in the Wendelstein 7-X stellarator *Nucl. Fusion* **62** 106005

[61] Alonso A. *et al* 2019 Understanding ion and impurity flows in the Wendelstein 7-X stellarator *Proc. 46th EPS Conf. on Plasma Physics* (*Milan, Italy*, *8–12 July 2019*) p I3.102 (available at: http://ocs.ciemat.es/EPS2019ABS/pdf/I3.102.pdf)

[62] Pavone A. *et al* 2019 Measurements of visible Bremsstrahlung and automatic Bayesian inference of the effective plasma charge Z_{eff} at W7-X *J. Instrum.* **14** C10003

[63] Kwak S. *et al* 2021 Bayesian inference of spatially resolved Z_{eff} profiles from line integrated bremsstrahlung spectra *Rev. Sci. Instrum.* **92** 043505

[64] Vano L. *et al* 2019 Studies on carbon content and transport with charge exchange spectroscopy on W7-X *Proc. 46th EPS Conf. on Plasma Physics* (*Milan, Italy*, *8–12 July 2019*) p P5.1065 (available at: http://ocs.ciemat.es/EPS2019ABS/pdf/P5.1065.pdf)

[65] Romba T., Reimold F., Jaspers R.J.E., Ford O.P., Vanó L. and Klinger T. 2023 Suppression of anomalous impurity transport in NBI-heated W7-X plasmas *Nucl. Fusion* **63** 076023

[66] Marushchenko N., Turkin Y. and Maassberg H. 2014 Ray-tracing code TRAVIS for ECR heating, EC current drive and ECE diagnostic *Comput. Phys. Commun.* **185** 165–76

[67] Zhang D. (The W7-X Team) 2021 Bolometer tomography on Wendelstein 7-X for study of radiation asymmetry *Nucl. Fusion* **61** 116043

[68] Pablant N.A. *et al* 2021 Correction and verification of x-ray imaging crystal spectrometer analysis on Wendelstein 7-X through x-ray ray tracing *Rev. Sci. Instrum.* **92** 043530

[69] Gradic D., Krychowiak M., König R., Henke F., Otte M., Perseo V. and Pedersen T.S. (W7-X Team) 2022 Impurity temperatures measured via line shape analysis in the island scrape-off-layer of Wendelstein 7-X *Plasma Phys. Control. Fusion* **64** 075010

[70] Hirsch M. *et al* 2019 ECE diagnostic for the initial operation of Wendelstein 7-X *EPJ Web Conf.* **203** 03007

[71] Pablant N.A., Bell R.E., Bitter M., Delgado-Aparicio L., Hill K.W., Lazerson S. and Morita S. 2014 Tomographic inversion techniques incorporating physical constraints for line integrated spectroscopy in stellarators and tokamaks *Rev. Sci. Instrum.* **85** 11E424

[72] Huang Z., Edlund E., Porkolab M., Bähner J.-P., Böttger L.-G., Sehren C.V., Stechow A.V. and Grulke O. 2021 The Wendelstein 7-X phase contrast imaging diagnostic *J. Instrum.* **16** P01014

[73] Huang Z. *et al* 2020 Turbulence studies in NBI heated discharges by the phase contrast imaging diagnostic in the Wendelstein 7-X stellarator *Proc. 47th EPS Conf. on Plasma Physics* (*Virtual*, *21 –25 June 2021*) p P2.1062 (available at: http://ocs.ciemat.es/EPS2021ABS/pdf/P2.1062.pdf)

[74] Connor J.W. 1988 Invariance principles and plasma confinement *Plasma Phys. Control. Fusion* **30** 619

[75] Petty C.C. *et al* 1995 Nondimensional transport scaling in DIII-D: Bohm versus gyro-Bohm resolved *Phys. Plasmas* **2** 2342–8